

1 **Probing mechanical selection in diverse eukaryotic genomes through accurate prediction of 3D
2 DNA mechanics**

3 Jonghan Park^{1,2}, Galina Prokopchuk^{3,4}, Andrew R. Popchock⁵, Jingzhou Hao^{2,6}, Ting-Wei Liao^{2,6},
4 Sophia Yan^{2,7}, Dylan J. Hedman⁸, Joshua D. Larson⁸, Brandon K. Walther^{2,9,10}, Nicole A. Becker¹¹,
5 Aakash Basu¹², L. James Maher III¹¹, Richard J. Wheeler¹³, Charles L. Asbury⁸, Sue Biggins⁵, Julius
6 Lukeš^{3,4} and Taekjip Ha^{2,6,9,10,*}

7 ¹College of Medicine, Yonsei University, Seoul, Republic of Korea

8 ²Howard Hughes Medical Institute and Program in Cellular and Molecular Medicine, Boston Children's
9 Hospital, Boston, MA, USA

10 ³Institute of Parasitology, Biology Centre, Czech Academy of Sciences, České Budějovice, Czech
11 Republic.

12 ⁴Faculty of Science, University of South Bohemia, České Budějovice, Czech Republic.

13 ⁵Basic Sciences Division, Howard Hughes Medical Institute, Fred Hutchinson Cancer Research Center,
14 Seattle, WA, USA

15 ⁶Department of Biophysics, Johns Hopkins University. Baltimore, MD, USA

16 ⁷Newton South High School, Newton, MA, USA

17 ⁸Department of Neurobiology & Biophysics, University of Washington, Seattle, WA, USA.

18 ⁹Division of Genetics and Genomics, Boston Children's Hospital, Boston, MA, USA

19 ¹⁰Department of Pediatrics, Harvard Medical School, Boston, MA, USA

20 ¹¹Department of Biochemistry and Molecular Biology, Mayo Clinic College of Medicine and Science,
21 Rochester, MN, USA.

22 ¹²Department of Biosciences, Durham University, Durham, United Kingdom.

23 ¹³Biological Sciences, University of Edinburgh, Edinburgh, Scotland, United Kingdom.

24

25

26 *To whom correspondence should be addressed (taekjip.ha@childrens.harvard.edu).

27

28

29 **Abstract**

30 Connections between the mechanical properties of DNA and biological functions have been speculative
31 due to the lack of methods to measure or predict DNA mechanics at scale. Recently, a proxy for DNA
32 mechanics, cyclizability, was measured by loop-seq and enabled genome-scale investigation of DNA
33 mechanics. Here, we use this dataset to build a computational model predicting bias-corrected intrinsic
34 cyclizability, with near-perfect accuracy, solely based on DNA sequence. Further, the model predicts
35 intrinsic bending direction in 3D space. Using this tool, we aimed to probe mechanical selection - that
36 is, the evolutionary selection of DNA sequence based on its mechanical properties - in diverse
37 circumstances. First, we found that the intrinsic bend direction of DNA sequences correlated with the
38 observed bending in known protein-DNA complex structures, suggesting that many proteins co-
39 evolved with their DNA partners to capture DNA in its intrinsically preferred bent conformation. We
40 then applied our model to large-scale yeast population genetics data and showed that centromere DNA
41 element II, whose consensus sequence is unknown, leaving its sequence-specific role unclear, is under
42 mechanical selection to increase the stability of inner-kinetochore structure and to facilitate centromeric
43 histone recruitment. Finally, *in silico* evolution under strong mechanical selection discovered
44 hallucinated sequences with cyclizability values so extreme that they required experimental validation,
45 yet, found in nature in the densely packed mitochondrial(mt) DNA of *Namystynia karyoxenos*, an ocean-
46 dwelling protist with extreme mitochondrial gene fragmentation. The need to transmit an
47 extraordinarily large amount of mtDNA, estimated to be > 600 Mb, in combination with the absence of
48 mtDNA compaction proteins may have pushed mechanical selection to the extreme. Similarly extreme
49 DNA mechanics are observed in bird microchromosomes, although the functional consequence is not
50 yet clear. The discovery of eccentric DNA mechanics in unrelated unicellular and multicellular
51 eukaryotes suggests that we can predict extreme natural biology which can arise through strong
52 selection. Our methods offer a way to study the biological functions of DNA mechanics in any genome
53 and to engineer DNA sequences with desired mechanical properties.

54

55

56 Present-day genomes are layered with multiple ‘codes’, including the genetic code in protein-
57 coding regions, transcription factor motifs in regulatory regions, genomic code for nucleosome
58 positioning and a histone code. Might there be another layer of ‘mechanical code’ where specific DNA
59 sequences and chemical modifications directly influence biological functions through DNA mechanical
60 properties^{1,2}? Previously, we extended the DNA cyclization assay, first developed in 1981³, to single-
61 molecule resolution and reported a profound effect of sequence on cyclization rate, which is a
62 measurable proxy for DNA mechanics such as anisotropic bending propensity and intrinsic flexibility⁴.
63 Subsequently, loop-seq, a sequencing-based readout of single DNA cyclization, enabled genome-scale
64 quantification of intrinsic cyclizability⁵ and revealed highly rigid DNA near gene promoters and a
65 rigidifying effect of cytosine methylation^{1,5}. Based on loop-seq data, bioinformatics models have been
66 developed to predict cyclizability from sequence and infer DNA mechanics across key genomic
67 landmarks in diverse genomes⁶⁻⁹. But as we will show below, the existing models have limited accuracy,
68 did not correct for biases introduced during loop-seq, and did not consider spatial anisotropy in DNA
69 bending.

70 Here, we developed an approach to predict bias-corrected DNA cyclizability with > 95%
71 accuracy and to infer intrinsic bending direction from sequence alone. We demonstrate the power of the
72 approach in three novel applications: (1) spatial analysis to predict intrinsic bending direction, (2)
73 probing mechanical selection from population genetics, and (3) discovery of extreme naturally
74 occurring DNA mechanics from its *in silico* evolution.

75 Accurate cyclizability prediction

76 For reliable prediction of the mechanical properties of DNA of any sequence, we need a large
77 dataset linking DNA sequence to its mechanics. A proxy for DNA mechanics, intrinsic cyclizability,
78 abbreviated as C0, was previously determined using loop-seq (Fig. 1a, Supplementary Fig. 1)⁵. C0
79 values of several libraries containing more than 150,000 50-bp sequences, randomly generated or
80 derived from the yeast genome, are currently the standards against which the performance of sequence-
81 to-cyclizability prediction is evaluated⁶⁻⁹. Because low sequencing read counts reduced the accuracy of
82 some C0 measurements (Supplementary Fig. 2), we removed C0 values of high uncertainty caused by
83 low read counts (Methods, Supplementary Fig. 3). Using the refined dataset, our deep-learning
84 approach achieved a Pearson’s correlation of ~0.96 between measured and predicted C0 (Fig. 1b,
85 Supplementary Fig. 4), much above the previous analyses whose maxima were 0.75~0.77 (Fig. 1c).

86 Loop-seq requires a pair of adapter sequences attached to the ends of the variable sequences
87 (50 bp in most studies, Fig. 1d, Supplementary Fig. 1). The adapters can create bias by bending
88 synergistically with the variable sequence. Indeed, C0 shows relatively weak correlation between the
89 original sequences and their reverse complement (Fig. 1e)⁵, likely because the swapped adapter
90 sequences impose a different mechanical context. Therefore, we devised a mathematical correction to
91 remove the contribution of the adapter sequences (Methods, Supplementary Fig. 5). This improved the
92 Pearson’s correlation of the cyclizability between the original sequence and its reverse complement to
93 0.97 from 0.89 (Fig. 1e, f). We termed C0 after the correction ‘adapter-corrected intrinsic cyclizability’,
94 C0_{corr}, which should be a quantity independent of its mechanical context. More specifically, C0_{corr} is
95 independent of sequence orientation (Fig. 1f) and rotational phasing (Supplementary Fig. 5c). Thus, we
96 will henceforth use ‘cyclizability’ to refer to adapter-corrected intrinsic cyclizability (C0_{corr}). Lastly, we
97 developed heuristic algorithms to enhance the speed of cyclizability predictions across genomic datasets
98 spanning multiple Gbps (Supplementary Note 8).

99 Spatial analysis reveals intrinsic bending direction

100 Because loop-seq was performed with DNA tethered to a bead surface, for sequences that
101 prefer to bend toward the tethering point, steric hindrance will lower their apparent cyclizability (Fig.
102 2a)⁵. In a previous study, loop-seq analyses with three different tether positions were implemented to
103 account for this effect and yielded intrinsic cyclizability C0, which is independent of tether position⁵.
104 Using the same dataset but after correcting for the adapter effects, we developed a ‘spatial analysis’
105 which allowed us to predict the preferred direction of bending at every position on the DNA (Methods).
106 As an example, for the well-positioned nucleosomes in budding yeast (*Saccharomyces cerevisiae*) *in*
107 *vivo*¹⁰, we found that the preferred bending direction of their wrapped DNA is towards the center of the
108 nucleosome (Fig. 2b, see red lines overlaid on nucleosome structure), suggesting that nucleosomes in
109 yeast favors genomic DNA with static bending directions that are compatible with the sharply bent DNA
110 conformations found in nucleosome structures¹¹.

111 Is it possible that highly bent DNA molecules in known protein-DNA structures intrinsically
112 prefer to bend in the same direction? A spectacular affirmative example is the BldC protein of
113 *Streptomyces* that bends DNA spirally (Fig. 2c)¹². Intrinsic bending direction overlaid on the structure
114 matches the observed DNA bending. A second example is EBNA1 of Epstein-Barr virus that bends
115 DNA in the direction of its intrinsic bending propensity (Fig. 2d)¹³. A third example is RAG1/2
116 recombinase where the deformation of 23 bp recombination signal sequence for V(D)J recombination
117 agrees with intrinsic DNA bending (Fig. 2e)¹⁴. We developed a convenient web interface for users to
118 enter the PDB ID of a structure and interactively visualize intrinsic bending directions overlaid with the
119 structure (Methods).

120 For a systematic investigation, we performed spatial analysis for 778 structures that contain
121 dsDNA molecules with well-defined DNA sequence in the RCSB database¹⁵ (Methods). We compared
122 the predicted 3D mechanics of DNA sequences used in the structural studies with those of randomly
123 generated DNA of the same length (Fig. 2f) by calculating a similarity score: the inner product between
124 vectors for the intrinsic bending direction and the observed bending direction (Fig. 2g, Methods). A
125 positive similarity score implies that the observed bending is favored by intrinsic DNA mechanics. We
126 found that DNA sequences used for experimental structural determination have higher similarity scores
127 compared to random DNA (Fig. 2h), especially when the observed structure has strong DNA bending
128 (top 30%, $P < 10^{-229}$, Fig. 2i, right), but the effect is still significant for structures with low DNA bending
129 (bottom 30%, $P < 10^{-132}$, Fig. 2i, left). Even when we divided the structures into nucleosomes (n=140),
130 transcription factors (n=275), and all others (n=322), the similarity score was higher for the DNA
131 sequences used for structural determination compared to random DNA sequences for each group
132 (Supplementary Fig. 6a). Therefore, available structures have a significant bias in favor of sequences
133 with predicted intrinsic bending direction that matches the observed bending direction. Such biases
134 were dependent on the structural category, largest for nucleosomes ($P < 10^{-167}$), smallest for
135 transcription factors ($P < 10^{-17}$), and the remainder intermediate ($P < 10^{-74}$) among the top 30% most
136 bent DNA structures (Supplementary Fig. 6a). Overall, our spatial analysis applied to the available
137 structures suggests that many proteins co-evolved with their DNA partners to recognize and bend DNA
138 sequences according to their intrinsic bending direction.

139 Can some of the biases be due to ‘selection’ by the researchers, for example, due to increased
140 stability of complexes that facilitates structural analysis? The answer seems to be yes for the nucleosome
141 structures because the average similarity score for deposited nucleosome structures has increased over
142 time (Fig. 2j). Indeed, there is a strong positive correlation between the similarity score and salt stability
143 of nucleosomes¹⁶ (Fig. 2k). The first reported nucleosome structure used alpha-satellite DNA¹¹ with
144 negative similarity scores near the dyad (Supplementary Fig. 6b). In contrast, Widom 601 DNA¹⁷,
145 widely adopted for more recent studies¹⁸⁻²⁰, has positive similarity scores in almost all positions
146 (Supplementary Fig. 6c). Higher similarity scores on the left side of Widom 601 DNA might explain
147 the asymmetrical unwrapping of nucleosome DNA under tension²¹ (Supplementary Fig. 6c). Also,

148 NCP-601L with uniformly high (Supplementary Fig. 6d) and NCP-146b with uniformly low similarity
149 scores (Supplementary Fig. 6e) are also the nucleosomes with the highest and the lowest nucleosome
150 stability against salt titration, respectively (Fig. 2k)¹⁶.

151 Probing mechanical selection from population genetics

152 If certain mechanical properties are disfavored due to functional constraints, sequence variants
153 responsible will rarely become fixed in natural populations. Borrowing from tools to quantify selection
154 pressure on sequence variants in protein coding²² and non-protein coding elements^{23,24}, we developed a
155 method to quantify selection pressure acting on DNA mechanics from population genetics data (Fig. 3a,
156 Methods) and applied it to the centromeric sequences of 1,011 isolates of *S. cerevisiae*²⁵.

157 After aligning the genome sequences of the 1,011 isolates at the 16 centromeres, we created,
158 for each 50 bp window, a simulated sequence that matches the Hamming distance of the corresponding
159 natural sequence from the consensus sequence (Fig. 3a, Methods). We compared cyclizability
160 distributions to determine whether variations found in natural sequences deviate significantly from the
161 simulated sequences. For example, significantly lower cyclizability in the natural sequences suggests
162 that any mutation increasing cyclizability, thus reducing DNA rigidity, was deleterious, leading to ‘pro-
163 rigidity selection’.

164 The centromere DNA is a site of kinetochore assembly which is critical for proper chromosome
165 segregation²⁶⁻²⁸. Each chromosome in *S. cerevisiae* has a single centromere with three centromere
166 defining elements (CDEI, CDEII, and CDEIII)^{29,30}. CDEI and CDEIII contain the recognition sites of
167 centromere binding factors³¹⁻³³ but the consensus sequence for CDEII has not been identified³⁴. CDEII
168 has high content of polymeric runs of A or T³⁴, and the longer A or T tracts were proposed to facilitate
169 the deposition of centromeric nucleosome containing Cse4^{CENP-A} by an unknown mechanism³⁵. We
170 found that the centromeric DNA is rigid (average $C_{0,\text{corr}} \sim -0.5$, Fig. 3b, top), possibly to prevent random
171 nucleosomes from occupying the centromeres³⁶. Averaged across all 16 centromeres, 1,011 yeast
172 isolates showed pro-rigidity selection at CDEI and the upstream portion of CDEII (Fig. 3b, bottom),
173 with a similar trend observed in individual centromeres (Fig. 3c).

174 As a further test, we examined CDEII bending in the inner-kinetochore structure³⁷ by
175 calculating the similarity score for the chromosome 3 centromere (CEN3) CDEII sequences of 1,011
176 yeast isolates. We found a positive similarity score in the region that curves around the centromeric
177 nucleosome, which overlaps with the downstream portion of CDEII (50 ~ 90 bp from the 5' end of
178 CDEI, Fig. 3d, top). The same region was under mechanical selection, accumulating variants with
179 positive similarity scores (Fig. 3d, bottom, Methods). Therefore, for centromere function, intrinsic DNA
180 mechanics in 3D, not just rigidity, appears to be under selection.

181 To probe the molecular basis underlying sequence-dependent centromere function, we
182 measured the recruitment of the histone H3 centromeric variant Cse4 to CEN3 under a perturbation of
183 DNA mechanics using single molecule fluorescence colocalization microscopy (Fig. 3e, Methods)³⁵.
184 We prepared the wild type CEN3 and three natural mutants by selecting three variants among the natural
185 population. The variants contained 4 to 7 mutations in CEN3 CDEII that preserve DNA mechanical
186 properties. We also generated three mutants that contain the same number of mutations but do not
187 preserve DNA mechanical properties (Fig. 3f, g, Supplementary Table 1). All three mechanics-
188 preserving natural variants recruited Cse4 to a similar level as the wild type whereas all three
189 cyclizability-changing mutants showed significantly reduced recruitment (Fig. 3h, i), supporting the
190 importance of CDEII mechanics in Cse4 recruitment. As a control, an earlier step, the recruitment of
191 Ndc10 to CDEIII, was unaffected by the change in CDEII mechanics (Supplementary Fig. 7a, b). Taken

192 together, our mechanical selection analysis showed that the centromeric element CDEII has evolved to
193 maintain specific mechanical properties important for kinetochore assembly.

194 ***In silico* evolution of DNA mechanics**

195 To understand how desired mechanical properties may emerge from selection, we adopted the
196 strong-selection weak-mutation approach³⁸, previously used to link promoter sequence to gene
197 expression in *S. cerevisiae*²⁴. Starting from a 50 bp sequence chosen at random, all possible single
198 substitutions were considered in each cycle to produce a total of 150 new sequences. The sequence with
199 the highest and lowest predicted $C_{0,\text{corr}}$ value were chosen in cyclizability-maximizing or minimizing
200 selection, respectively, while one of the 150 sequences was randomly picked to simulate genetic drift.
201 The chosen sequence serves as an input for the subsequent cycle of simulation (Fig. 4a).

202 In the genetic drift simulation, $C_{0,\text{corr}}$ diverged as mutations accumulated (Fig. 4b), and even
203 two rounds of single point mutation were sufficient to change $C_{0,\text{corr}}$ by 0.77 in some sequences, which
204 is nearly three times the standard deviation of the initial $C_{0,\text{corr}}$ distribution. In parallel, a series of
205 maximizing and minimizing selections shifted the overall distributions of $C_{0,\text{corr}}$ toward the
206 corresponding extrema (Fig. 4c). Thus, selection pressure can readily alter cyclizability with just a few
207 mutations.

208 Continued directional selection until the 50th step created artificial DNA sequences having
209 extreme cyclizability that rarely exist in our dataset, likely because of deep network hallucination³⁹ (Fig.
210 4c). During the selection, poly(dA:dT) tracts accumulated with lengths converging to 6 or 11 bp (half
211 or single helical turn) that are positioned in phase along helical repeats (Supplementary Fig. 8)
212 consistent with the model where phased repeats of (dA₅₋₆:dT₅₋₆) tracts can cause static bends to add up
213 or cancel each other out depending on the relative phase⁴⁰⁻⁴². We experimentally measured the kinetics
214 of these sequences using single-molecule cyclization⁴ (Methods) and confirmed that the DNA sequence
215 with the highest $C_{0,\text{corr}}$ rapidly looped (~90% within 5 minutes), but the DNA with the lowest $C_{0,\text{corr}}$
216 hardly formed loops (~10% after an hour, Fig. 4d). Atomic force microscopy (AFM) images of 600 bp
217 sequences derived from *in silico* evolved sequences of the large positive and negative $C_{0,\text{corr}}$ values
218 showed wavy structures and straight structures (Fig. 4e), respectively, with the corresponding curvature
219 being much larger for the more cyclizable sequence (Fig. 4f).

220 To what extent do sequence-encoded DNA physical properties dictate protein-DNA
221 interactions? It is important to reflect on the facts that cells have developed approaches to increase
222 apparent DNA flexibility by the activities of both site-specific and site non-specific architectural DNA
223 kinking proteins^{43,44}. Proteins that contain one or more high-mobility group boxes (HMGB) are believed
224 to play roles in DNA compaction. We therefore tested the DNA-bending ability of HMGB containing
225 proteins, Nhp6A and HMGB1 (Methods). Remarkably, the extremely rigid DNA discovered via *in silico*
226 evolution, which rarely cyclized even after 1 hour, showed greatly accelerated cyclization in the
227 presence of Nhp6A or HMGB1 proteins (Fig. 4g). This result is an important reminder that architectural
228 DNA-binding proteins can overcome intrinsic DNA physical properties.

229 **Eccentric mechanics of mitochondrial DNA of diplonemid protists**

230 Despite the experimental validation of *in silico*-engineered DNA of extreme mechanics, we
231 initially presumed that these artificial sequences, which required very strong selection over many rounds,
232 would not appear in nature. Therefore, we were surprised when nucleotide BLAST⁴⁵ search using the
233 hallucinated sequence with the highest $C_{0,\text{corr}}$ found matches in the database of natural DNA sequences.
234 Most of the matches were to the non-coding regions of mitochondrial genomes of *Namystynia*

235 *karyoxenos* and *Hemistasia phaeocysticola*, both from Hemistasiidae, diplomonmid protists living in the
236 ocean (Supplementary Fig. 9a-c, Methods). The mitochondrial DNA (mtDNA) of diplomonmids has a
237 highly unusual architecture, with genes fragmented into small modules contained on different, non-
238 catenated circular chromosomes that consist mostly of noncoding DNA. Transcription of these gene
239 modules occurs independently, and after editing the transcripts are *trans*-spliced together, assembling
240 the modules into mature mRNAs⁴⁶. Sequence similarity between the non-coding region defines classes
241 of mtDNA from A to Q, X, or U (unclassified)⁴⁶.

242 We observed higher average cyclizability in the non-coding regions in the mtDNA of
243 Hemistasiidae, compared to other diplomonmids (Fig. 4h), which is due to the accumulation of
244 poly(dA:dT) tracts in a specific pattern. For example, the highly cyclizable motif, 5'-GGGCCAAAAAA-
245 3', is present in the mtDNA of *H. phaeocysticola* with moderate frequency, while this motif greatly
246 expanded its prevalence in *N. karyoxenos* (Supplementary Fig. 9d). This repeating motif was previously
247 reported as an unorthodox characteristic that defines class X of mtDNA⁴⁶. AFM imaging of 600 bp
248 DNA derived from the mtDNA X031 of *N. karyoxenos* (Supplementary Fig. 9e, Supplementary Table
249 1) revealed wavy structures (Fig. 4e) with elevated curvature value (Fig. 4f), resembling the *in silico*-
250 engineered sequence with extremely high cyclizability.

251 Unlike classical diplomonmids that have reached a plateau in their complexity of gene
252 fragmentation, hemistasiids have evolved additional gene fragmentation with twice the number of
253 modules (Fig. 4h). Gene fragmentation, transcriptional, and post-transcriptional modification and
254 regulation with substantial complexity may necessitate a large copy number of mtDNA as part of a
255 mechanism to ensure the transmission of each module to subsequent generation without loss. Using
256 transmission electron microscopy of *N. karyoxenos* we observed the presence of extraordinarily large
257 amount of mtDNA, organized as strips of electron-dense beads within the organellar lumen (Fig. 4i).
258 To quantify the total amount of mtDNA in this organism, we used propidium iodide (PI) because, unlike
259 Hoechst 33342, its DNA straining is independent of DNA cyclizability (Supplementary Fig. 10a).
260 Fluorescence intensity of PI staining after segmentation of nucleus volume from phase contrast images
261 revealed that approximately 2/3 of total cell DNA is extra-nuclear (Fig. 4j, k, Methods). In the absence
262 of nuclear genome size estimates for *N. karyoxenos*, we used the 280 Mb-haploid nuclear genome of
263 the closely related *P. papillatum*⁴⁷ as a proxy. This approximation led to an estimated ~653 Mb mtDNA
264 in the single mitochondrion of *N. karyoxenos*, which would qualify it as the largest amount of extra-
265 nuclear DNA known so far with the previous record being approximately ~260 Mb mtDNA⁴⁸. To
266 provide some context, in a typical human cell, numerous mitochondria combined contain ~1000 times
267 less DNA than the nucleus (~8.3 Mb vs ~6.4 Gb)⁴⁹. We confirmed the abundant presence of highly
268 cyclizable sequences in mitochondria by fluorescence *in situ* hybridization (Supplementary Fig. 10b).

269 In this study, we showed that proteins that contain HMGB make even the extremely rigid
270 sequences cyclizable as rapid as the most cyclizable sequences (Fig. 4g), and HMGB proteins are found
271 in the mitochondria of most organisms^{50,51}, for example, Abf2p in yeast⁵² and TFAM in mammals⁵³.
272 Therefore, there may be no need for extremely cyclizable sequences as long as mtDNA compacting
273 proteins exist. Publicly available genomic sequences of *N. karyoxenos*
(<https://www.ncbi.nlm.nih.gov/sra/SRX5472374> and <https://www.ncbi.nlm.nih.gov/sra/SRX5434880>)
275 allow us to speculate which proteins implicated in mtDNA packaging are present. The search in the *de*
276 *novo* assembly of the RNA-seq data⁵⁴ did not identify any mtDNA-associated histone-like proteins
277 (KAPs), which are the only known ones possibly involved in packaging mtDNA in these and related
278 protists⁵⁵. Extending our search to all other diplomonmid sequences, including the high-quality nuclear
279 genome of *P. papillatum*⁴⁷, and using KAP1 through KAP4 of *Crithidia fasciculata* as queries failed to

280 identify their putative homologs, allowing us to conclude that we could not identify any mtDNA binding
281 proteins in diplonemids. Therefore, we suggest that the requirement to pack an extraordinarily large
282 amount of DNA into a small volume of single mitochondrion in the absence of mtDNA compacting
283 protein may have caused the accumulation of extremely cyclizable sequences in *N. karyoxenos*. In fact,
284 existing mutations around the 50 bp consensus sequence with extreme cyclizability rarely drop $C_{0\text{corr}}$
285 below 2 in *N. karyoxenos* (only 0.15% of the time) whereas random mutations with the same Hamming
286 distance from the consensus sequence can lower $C_{0\text{corr}}$ below 1 (Supplementary Fig. 9f, Methods).
287 Therefore, the native repeats have undergone mechanical selection to preserve high cyclizability of
288 mtDNA .

289 To seek other examples of natural DNA of extreme mechanics, we ran BLAST search using a
290 highly cyclizable mtDNA motif from *Artemidina motanka*, a close relative of *N. karyoxenos* and *H. phaeocysticola*⁵⁶, and found matches to bird genomes, specifically their microchromosomes (see
291 regions of house finch chromosome 39 and common parakeet chromosome 30 with cyclizability
292 frequently exceeding 2) (Fig. 4l, Supplementary Fig. 11a). Of note, the closest outgroup, American
293 alligator, did not show extreme cyclizability in its smallest chromosome (Supplementary Fig. 11b).
294 Interestingly, we observed a strong anticorrelation between chromosome-averaged cyclizability and
295 chromosome size in house finch (*Haemorhous mexicanus*) (Fig. 4m), and 59 other bird species (Fig.
296 4n) suggesting that there was a selection pressure to enrich for highly cyclizable sequences in tiny
297 chromosomes in the bird lineage although we do not know the biological processes that the observed
298 mechanical selection operated on. Overall, our discovery of extreme DNA mechanics in two unrelated
299 lineages of uni- and multicellular eukaryotes of life suggests that our *in silico* method identified extreme
300 biology and provides examples of nature finding a way to use even extremely eccentric DNA mechanics.
301

302 Discussion

303 We significantly increased the accuracy of cyclizability prediction over prior methods by (1)
304 removing DNA with low sequencing read counts, (2) mitigating the effect of adapter sequences, and (3)
305 avoiding learning the cyclizability of DNA with Nt.BspQ1 nickase recognition motifs (Fig. 1, Methods).
306 Predictions of DNA looping at a near-perfect accuracy will help link DNA mechanics to the function of
307 genomic elements and understanding the evolution of DNA mechanics.

308 Phased (dA₅₋₆:dT₅₋₆) tracts accumulated during the *in silico* evolution (Supplementary Fig. 8)
309 can explain the fluctuations of G/C contents or poly(dA:dT) tracts reported in genomic elements of
310 many bacteria and eukaryotes where certain DNA mechanical properties are desired, e.g.,
311 *Saccharomyces* nucleosomes¹⁰, transcription start sites⁵⁷, centromeres³⁴, replication origins⁵⁸, mtDNA
312 of trypanosomes^{59,60}, *E. coli* DNA gyrase cleavage sites⁶¹ and *Streptomyces* BldC binding motifs¹².

313 Selection against mutations that disrupt the functionally important mechanical properties can
314 in principle be quantified by examining mechanical features of sequences found in the genetic pool.
315 Here, our investigation based on population genetics data of 1,011 yeast isolates identified their
316 centromeres as a region with mechanical selection, likely due to unique mechanical properties under
317 selection for inner kinetochore stability (Fig. 3). This introduces a new possibility to apply a similar
318 method to diverse species, including humans, and relate DNA mechanics to phenotypes or diseases.

319 MtDNA occurs in nucleoids, and numerous nucleoid-associated proteins have so far been
320 identified^{50,51}. The consensus is that in the yeast mitochondrion, DNA is wrapped only by Abf2p⁵²
321 thanks to its two HMGB boxes, each of which induces a sharp 90° bend⁶². The composition of
322 mammalian mitochondrial nucleoid is still unclear, but TFAM, the HMGB boxes of which intercalate

323 into the minor groove in sequence-unspecific manner⁵³, compacts DNA by bending the DNA backbone
324 and DNA loop formation until the DNA is fully compacted⁶³. This is the same mechanism utilized by
325 yeast Nhp6A and mammalian HMGB1 proteins tested here (Fig. 4g). The amplification of mtDNA in
326 *N. karyoxenos* (Fig. 4i-l, Supplementary Fig. 10) and in other diplonemids⁴⁸ may have required extreme
327 mtDNA compaction, which can be achieved through DNA-bending proteins or by selection for DNA
328 sequences with intrinsic properties that make them highly cyclizable. We propose that diplonemids
329 evolved along the latter path; exploiting highly cyclizable mtDNA to store amplified mtDNA in the
330 absence of DNA-bending proteins.

331

332 Methods

333 Uncertainty of loop-seq measured cyclizability

334 Variables were defined as follows. N , the total number of aligned reads of DNA molecules in a library, n , the
335 number of aligned reads to a target DNA sequence, C , cyclizability. The lower-case c and s stand for control (no
336 digestion) and sample (sequenced after digestion of unlooped DNA). Cyclizability determined by loop-seq is
337 $\log((n_s/N_s)/(n_c/N_c))$ (Supplementary Note 1).

338 Bayesian statistics with an uninformative Jeffreys prior yields a probability distribution of cyclizability.

$$339 P(C) \sim (e^{2C} + 1)^{\frac{1}{2}} e^{C(n_s - \frac{1}{2})} (N_c + N_s e^C)^{-(n_c + n_s)}$$

340 The 95% confidence interval (CI) of cyclizability is determined as $C_{lower} < C < C_{upper}$, where $P(C < C_{lower}) = 0.025$ and $P(C_{upper} < C) = 0.025$. Similarly, the uncertainty score calculated using frequentist
341 statistics is as follows.

$$343 \frac{1}{\sqrt{n_c}} + \frac{1}{\sqrt{n_s}} + \frac{1}{\sqrt{n_c n_s}}$$

344 Here, we use, interchangeably, the 95% CI determined using Bayesian statistics and frequentist statistics
345 (Spearman's $R = 0.997$) to select a sub-dataset for model training and testing. See Supplementary Note 2 for details
346 on the development of the formula.

347

348 Model architecture

349 Models that share a single deep learning architecture (Supplementary Fig. 3a) were trained individually on
350 different cyclizabilities (C0, C26, C29, and C31 etc. where the numeric values denote the positions of biotin used
351 for tethering DNA molecules to a bead surface). The models were implemented using Keras⁶⁴.

352 Input (200,) - A 50 bp DNA is converted into a 200-dimensional vector by one-hot encoding:

353 A: [1, 0, 0, 0], T: [0, 1, 0, 0], G: [0, 0, 1, 0], C: [0, 0, 0, 1]

354 First 1D convolution layer - Kernel size: 28, Output channels: 64, Stride: 4, Output shape: (44, 64). A bias term
355 and a rectified linear unit (ReLU) activation were added.

356 Second 1D convolution layer - Kernel size: 33, Output channels: 32, Output shape: (12, 32). A bias term and a
357 rectified linear unit (ReLU) activation were added.

358 Flatten layer - Output shape: (384,).

359 First fully connected layer - Output shape: (50,). A bias term and a rectified linear unit (ReLU) activation were
360 added. The layer was L2 regularized with the regularization constant of 0.001.

361 Second fully connected layer (output) - Output shape: (1,). This layer predicts cyclizability of a 50 bp DNA
362 sequence.

363

364 Training the model

365 Training datasets for C26, C29, or C31 consist of sequences from the Tiling library⁵ selected by their uncertainty
366 score of measured C values lower than 0.1. C0 was trained using sequences that are shared in the three datasets
367 used for training C26, C29, and C31. The testing datasets were selected in the same way from sequences in the
368 ChrV library⁵. Sequences containing the digestion motifs of the endonuclease Nt.BspQ1, 5'-GAAGAGC-3' or 5'-
369 GCTCTTC-3', were removed from all datasets, because the unintended nicks produced in the variable 50 bp DNA
370 during the loop-seq protocol increase C values. The effect of the digestion motif on cyclizability was previously
371 reported and interpreted erroneously as being caused by changes in DNA mechanics⁷. Unless otherwise stated,
372 models were trained to minimize a mean squared error loss for seven epochs using the Adam optimizer⁶⁵, with an
373 initial learning rate of 0.001 and decay rates β_1 and β_2 of 0.9 and 0.999, respectively. The computational details
374 are described in Supplementary Note 3.

375

376 Removing the effects of adapter sequences

377 The upper envelopes $U(n)$ of the oscillatory patterns of $C(n)$ on a sufficiently long DNA were acquired by
378 cubic interpolations of local maxima using the interp1d function of Python SciPy 1.9.3⁶⁶ (Supplementary Fig. 5),
379 where n is the position of biotin tether (26, 29, or 31). A cyclizability value is considered a local maximum if the
380 value is the highest among a set of 7 consecutive cyclizability values (including itself, three values to the left and
381 three values to the right). The process is similarly done to find lower envelopes $L(n)$.

382 The corrected upper envelope U_0 and the mock amplitude A' (in which the difference between $U(n)$ is
383 absorbed) that fits to the formula below are calculated using the fsolve function of Python SciPy 1.9.3⁶⁶
384 (Supplementary Fig. 5a).

$$385 \quad U(n) = U_0 + A' \cos\left(\frac{60.5 - n}{10.3} * 2\pi - \frac{2}{3}\pi - \varphi'\right)$$

$$386 \quad L(n) = L_0 + A'' \cos\left(\frac{60.5 - n}{10.3} * 2\pi - \frac{2}{3}\pi - \varphi''\right)$$

387 The adapter-corrected cyclizability is defined accordingly.

$$388 \quad C(n)_{corr} := \begin{cases} L_0 + (C(n) - L(n)) * \frac{U_0 - L_0}{U(n) - L(n)}, & n = 26, 29, 31 \\ \boxed{} \\ \frac{U_0 + L_0}{2}, & n = 0 \end{cases}$$

389 C0_{corr}, C26_{corr}, C29_{corr}, and C31_{corr} were calculated at a base resolution for yeast ChrV. We selected 576,647 50 bp
390 windows with clearly defined adapter-corrected cyclizability values. This selection excluded the first and last 50
391 windows, as well as any windows with a corrected upper envelope lower than the corrected lower envelope. The
392 selected data were used for learning over four epochs with the same model hyperparameters stated in the previous
393 section (Supplementary Fig. 3a). The model predicted adapter-corrected cyclizability with high accuracies in
394 testing datasets that are not used for model training (Pearson's R > 0.96, Supplementary Fig. 5e). The
395 computational details are described in Supplementary Note 4.

396

397 Aligning genomic sequences of 1,011 yeast isolates

398 We aligned the genomic sequences of 1,011 isolates of *S. cerevisiae*²⁵ to a region of interest using the BLAST-
399 like alignment tool (BLAT)⁶⁷. Template DNA sequences were obtained from the sacCer3 reference genome⁶⁸. Any
400 alignments with less than 80% identity to the reference, as well as those containing ambiguous nucleotides or
401 indel mutations, were excluded. To avoid including excessively duplicated regions in our dataset, we excluded
402 genomic regions with more than 1.2×1,011 alignments, in accordance with the process outlined in a previous
403 study²⁴. Aligning the genomic sequences in centromeres is outlined in Supplementary Note 7.

404

405 Quantifying selection pressure on DNA mechanics

406 We quantified mechanical selection based on population genomes aligned to a region of interest²⁵. For each 50 bp
407 window, simulated sequences were generated from the natural alignments with random mutations, such that
408 Hamming distance from the consensus sequence is identical in both sets (Fig. 3a). Hamming distance of a 50 bp
409 DNA is the minimal number of point mutations required to create that 50 bp DNA from the consensus sequence,
410 and the consensus sequence is the DNA sequence in which the most frequent base at each position is taken as the
411 consensus. Natural or simulated sequences identical to the consensus sequence were omitted from the analysis.
412 An identical mutant generating scheme was used to study the effect of native mutations in *N. karyoxenos* mtDNA
413 (Supplementary Fig. 9f).

414 We predicted C0_{corr} of natural and simulated 50 bp sequences. As yeast isolates share a common ancestor, natural
415 alignments consist of groups of homogeneous 50 bp sequences. Accordingly, we set the variables as follows,
416 assuming that there are n different natural C0_{corr} values (i is an integer ranging from 1 to n). c_i : Counts of
417 natural isolates with identical DNA sequence i . N : Total counts of simulated sequences. r_i : Rank of each natural
418 C0_{corr} among simulated C0_{corr}. $S = \sum c_i r_i$ ($\hat{S} = \sum c_i \hat{r}_i$ for observed ranks). The rank of 0 is assigned to a natural
419 sequence if it has the lowest C0_{corr} among simulated C0_{corr}.

420 As an analogue of Z value from normal distribution, Z -score of mechanical selection is determined.

421

$$Z = \frac{\hat{S} - E[S]}{(V[S])^{\frac{1}{2}}}$$

422 where $E[S] = N \sum c_i / 2$ and $V[S] = N(N + 2) \sum c_i^2 / 12$.

423 P -value of mechanical selection is determined as follows.

424

$$P(S \leq \hat{S}) = \frac{1}{2} + \frac{\alpha X}{\pi} \sum_{t=1}^{\infty} sinc(\alpha X t) sinc(\alpha N_1 t) \dots sinc(\alpha N_n t)$$

425 where $X = \sum S - E[S]$, $N_i = c_i N / 2$, $\alpha = \pi / (N_1 + \dots + N_n)$.

426 Here, *sinc* is defined as follows.

427

$$sinc(x) := \begin{cases} 0, & x = 0 \\ \frac{\sin x}{x}, & x \neq 0 \end{cases}$$

428 The statistics are valid only in 50 bp windows with enough diversity of natural sequences (Supplementary Note
429 6). We measured the diversity using information entropy.

430

$$H = -\left(\frac{m_i}{M}\right) \sum_{i=1}^k \log\left(\frac{m_i}{M}\right)$$

431 M is the total number of natural sequences, with k unique sequences each with m_i ($i = 1, \dots, k$) isolates ($M =$

432 $\sum m_i$). 50 bp windows with information entropy higher than 0.75 were used in further analyses. Reproducibility
433 and computational details are described in Supplementary Note 6.

434

435 **Spatial analysis of DNA bending**

436 $C_{26\text{corr}}$, $C_{29\text{corr}}$, and $C_{31\text{corr}}$ measure proficiencies of DNA looping in three different directions⁵. Taking advantage
437 of this, we inferred the rotational phase of DNA looping and its amplitude using a method that we named spatial
438 analysis.

439

$$C(n)_{corr} = C_{0\text{corr}} + A \cos\left(\frac{60.5 - n}{10.3} * 2\pi - \frac{2}{3}\pi - \varphi\right)$$

440 n is the position of biotin tether (26, 29, or 31). The values of $C_{26\text{corr}}$, $C_{29\text{corr}}$, and $C_{31\text{corr}}$, were adjusted by
441 subtracting constants to set the average of each cyclizability to 0 before use, because cyclizability values from
442 different loop-seq experiments can be compared up to a constant offset⁵. $C_{0\text{corr}}$, amplitude $A \geq 0$, and phase $\varphi \in$
443 $[-\pi, \pi]$, were then obtained using Python SciPy 1.9.3 package⁶⁶ with the starting estimate of [1, 1, 1]. The
444 amplitude A is a relative preference of bending in a certain direction indicated by the phase φ . For example, a
445 DNA molecule has no preference in bending direction when the amplitude is zero.

446 The formula assumes 10.3 bp for a helical turn of a duplex DNA, but the precise value may vary in different
447 contexts. Thus, when interpreting the results, we avoid relying excessively on the precise values of amplitude A
448 or phase φ . For a similar reason, $C_{0\text{corr}}$ obtained by spatial analysis was not used in model training or testing.
449 Verification of the method is described in Supplementary Note 5.

450 We repeat the process using Z-scores to see the mechanical selection in a 3-dimensional space.

451

$$Z_{C(n)_{corr}} = Z_{C_{0\text{corr}}} + A_Z \cos\left(\frac{60.5 - n}{10.3} * 2\pi - \frac{2}{3}\pi - \varphi_Z\right)$$

452 $Z_{C(n)_{corr}}$ are Z-score obtained by using $C(n)_{corr}$ instead of $C_{0\text{corr}}$, where n is the position of biotin tether (26, 29,
453 or 31). A_Z and φ_Z quantify the amplitude and the rotational phase of mechanical selection in a 3-dimensional
454 space, respectively. Computations to obtain A_Z and φ_Z using the formula above are done similarly as in the
455 spatial analysis based on cyclizability. Unlike cyclizability, the Z-scores were not normalized by subtracting their
456 average values before analysis, as the constant offsets between different types of cyclizability disappear during Z-
457 score computation.

458

459 **Visualizing DNA bending in a 3-dimensional space**

460 The main helical axis of a dsDNA molecule is defined by the midpoint of C6 of pyrimidine and C8 of purine
461 base⁶⁹. To visualize the intrinsic DNA bending at a base-base step, we drew an arrow perpendicular to the main
462 helical axis. The starting point of each arrow was set to the midpoint of the helical axis at a base-base step, and
463 the length (in angstroms) of each arrow represented the amplitude of DNA bending (obtained by spatial analysis)
464 multiplied by a factor of 30 unless otherwise noted. For each base-base step, a spatial analysis result from the 50
465 bp window that puts the base-base step in the middle (25 bp to the upstream and downstream) was used. For a
466 base-base step at the boundaries of a linear DNA, the average cyclizability of 200 DNA sequences with randomly
467 filled missing bases was used for spatial analysis.

468 The observed bending vector of a base-base step was defined by the difference between the unit vector
469 representing the direction of main helical axis at the last (between the 49th and 50th bases) and at the first (between
470 the 1st and 2nd bases) base-base step of the surrounding 50 bp window. The similarity between the intrinsic and the observed
471 bending was defined by the inner product of the vectors representing the intrinsic and the observed
472 bending. PDB structures generated by refining and fitting experimental data to other known PDB structures were
473 not included in our analysis at the RCSB database scale (Fig. 2) to avoid arbitrary DNA sequences being inserted

474 into the structures.

475

476 **Total internal fluorescent microscopy slide preparation for single molecule colocalization analysis of 477 centromere assembly**

478 Coverslips and microscope slides were ultrasonically cleaned and passivated with PEG as described previously³⁵.
479 Briefly, slides were ultrasonically cleaned and then treated with vectabond (Vector Laboratories) prior to
480 incubation with resuspended 1% (w/v%) biotinylated mPEG-SVA MW-5000K/mPEG-SVA MW-5000K (Lysan
481 Bio) in flow chambers made with double-sided tape. Passivation/functionalization was carried out overnight at
482 4 °C. After functionalization, flow chambers were washed with Buffer L (25 mM HEPES pH 7.6, 2 mM MgCl₂,
483 0.1 mM EDTA pH 7.6, 0.5 mM EGTA pH 7.6, 0.1 % NP-40, 175 mM K-Glutamate, and 15% Glycerol) and then
484 incubated with 0.3 M BSA/0.3M Kappa Casein in Buffer L for 5 min. Flow chambers were washed with Buffer
485 L and then incubated with 0.3M Avidin DN (Vector Laboratories) for 5 min. Flow chambers were then washed
486 with Buffer L and incubated with ~100 pM of respective CEN DNA template (Supplementary Table 1) for 5 min
487 and washed with Buffer L. For endpoint colocalization assays, flow chambers were filled with 100 µL of whole-
488 cell extract (WCE) containing protein(s) of interest via pipetting and wicking with filter paper. WCE was prepared
489 as previously described³⁵. After addition of WCE, slides were incubated for 90 min at 25°C and then WCE was
490 washed away with Buffer L. Flow chambers were then filled with Buffer L with oxygen scavenger system⁷⁰ (10
491 nM PCD/2.5 mM PCA/1mM Trolox) for imaging.

492

493 **Total internal fluorescent image collection and analysis**

494 Colocalization images were collected on a Nikon TE-2000 inverted RING-TIRF microscope with a 100× oil
495 immersion objective (Nikon Instruments) with an Andor iXon X3 DU-897 EMCCD camera. Images were
496 acquired at 512 px × 512 px with a pixel size of 0.11 µm/px at 10MHz. Atto-647 labeled CEN DNA templates
497 (Supplementary Table 1) were excited at 640 nm for 300 ms, GFP-tagged Cse4 was excited at 488 nm for 200 ms,
498 and mCherry-tagged Ndc10 was excited at 561 nm for 200 ms. Single snapshots of all channels were acquired,
499 and images were analyzed using ComDet v.0.5.5 plugin for ImageJ (<https://github.com/UU-cellbiology/ComDet>)
500 to determine colocalization and quantification between DNA channel (647 nm) and GFP (488 nm) and mCherry
501 (561 nm) channels. Results were quantified and plotted using MATLAB (The Mathworks, Natick, MA).
502 Adjustments to example images (contrast, false color, etc.) were made using FIJI⁷¹ and applied equally across
503 entire field of view of each image.

504

505 **Local alignment searching of DNA sequences with high cyclizability**

506 Matches of 5'-GCCAAAAAAGGGCCAAAAATGGCCATTGGCCCTTTTGCCTTT-3', the 50 bp
507 DNA with the highest C0_{corr} found after the 50th steps of *in silico* selections favoring higher C0_{corr} (Fig. 4c,
508 Supplementary Fig. 8e), were found using BLASTn search with the word size, match, and mismatch scores of 7,
509 1, and -1, respectively. Resulting hits were sorted by E-value (Supplementary Fig. 9a, b). C0_{corr} of mitochondrial
510 genomes, including those found by BLASTn search, were predicted after replacing ambiguous nucleotides with
511 random bases (Fig. 4h, Supplementary Fig. 9c).

512

513 **Ultrastructure of *Namystinia karyoxenos***

514 *N. karyoxenos* was cultivated in a nutrient-rich medium at 22 °C as previously described⁵⁶. The cells were
515 harvested during the exponential growth phase by centrifugation at 4,000 g for 30 min and then processed by
516 high-pressure freezing technique and freeze substitution as described elsewhere⁷². Subsequently, the samples were
517 observed using a JEOL 1400 transmission electron microscope at an accelerating voltage of 80 kV.

518

519 Quantification of mitochondrial DNA

520 Cells were harvested as described above and fixed with 4% paraformaldehyde in artificial seawater for 30 min at
521 room temperature (RT). After fixation, the paraformaldehyde was washed off with phosphate buffered saline
522 (PBS), and the cells were mounted onto gelatin-coated slides for adhesion. The air-dried slides were then
523 immersed in -20 °C methanol overnight for cell permeabilization, following which the cells were rehydrated in
524 PBS for 10 min and treated with RNase A (50 µg/mL) for 2 hrs at RT. Cells were then stained with a combination
525 of 5 µg/ml Hoechst 33342 (bisbenzimide) and 25 µg/ml propidium iodide (PI) for 10 min. Dyes were removed by
526 a wash in PBS and slides were mounted with ProLong Gold Antifade reagent (Invitrogen). Images were acquired
527 via a 100× objective lens on a BX63 Olympus widefield fluorescence microscope equipped with an Olympus
528 DP74 digital camera using CellSens Dimension software v. 1.11 (Olympus) and processed in Image J v. 1.52p
529 software. From micrographs of the PI fluorescence we first measured the background signal from the modal pixel
530 value of the field of view and subtracted it from the pixel values. We then identified and segmented the nucleus,
531 based on their constant size and internal structure in the PI image, and whole cell, from the phase contrast image.
532 The relative nuclear to total DNA quantity was measured from the ratio of integrated pixel values in the nucleus
533 and whole cell regions. As the cells are thin, we used widefield microscopy and a single focal plane, which
534 effectively integrates the fluorescent signal from the entire cell volume.

535 For in vitro measurement of Hoechst 33342 and PI fluorescent signal when bound to DNA of different
536 cyclizabilities, we generated double stranded (ds) DNA by annealing of a forward and reverse 100 base
537 oligonucleotides. 100 nM forward and reverse primer were mixed in annealing buffer (10 mM Tris-HCl, pH 8.0;
538 50 mM NaCl; 1 mM EDTA), and annealed by denaturation at 95°C for 2 min, followed by cooling to 25°C over
539 45 min. The dsDNA was diluted to 25 mM in annealing buffer with 5 µg/ml Hoechst 33342 and 25 µg/ml PI,
540 incubated at RT for 15 min, and fluorescence was measured at 544 nm excitation/620 nm emission (red
541 fluorescence) and 355 nm excitation/460 nm emission (blue fluorescence). Background signal from DNA-lacking
542 sample was measured and subtracted. All samples were generated and measured in technical triplicate.

543

544 Targeting the circularized regions of *N. karyoxenos* mtDNA

545 To detect circularized mtDNA sequence, we employed fluorescence in situ hybridization (FISH) in combination
546 with immunofluorescence (IF) assay to visualize the mitochondrion. The cells were fixed as described above,
547 washed and permeabilized using eBioscience buffer, and incubated overnight at 4° C with a rabbit antibody against
548 β chain of mitochondrial ATP synthase, diluted 1:500. The primary antibody was then removed, and the cells were
549 washed and incubated with a goat anti-rabbit secondary antibody conjugated to Alexa Fluor 488, diluted 1:1,000,
550 for 1 hour at RT in the dark. Next, the cells were washed and allowed to adhere onto gelatin-coated slides, while
551 being kept in the dark. The air-dried slides were then treated with 0.1% Triton X-100 for 5 min and washed with
552 PBS. Following this, the cells were infiltrated with a DNA probe (5'-Cy3-
553 CCAAAAAAGGGCCAAAATGGCC-3') that was resuspended in a hybridization buffer (70% formamide; 1×
554 saline sodium citrate (SSC) buffer pH 7.0; 10% dextran sulfate; 8 µg salmon sperm DNA; 50 ng DNA-Cy3 probe)
555 for 1 hr at RT. The samples were then denatured for 5 min at 85 °C and left for hybridization overnight in the dark
556 at 42 °C in a humid chamber. Afterwards, the samples were washed twice for 15 min with 70% formamide and
557 10 mM Tris-HCl, pH 7.2, at 42 °C and then 3× for 5 min with 1× SSC. Subsequently, the slides were mounted
558 with ProLong Gold antifade reagent (Invitrogen) containing Hoechst 33342 and examined by FV3000 confocal
559 laser scanning microscope (Olympus) with the spectral filter windows set as follows: for Hoechst channel 417-
560 486 nm, Alexa Fluor 488 505-537 nm, and for Cy3 549-584 nm.

561

562 Single-molecule fluorescence resonance energy transfer (smFRET) DNA cyclization assay

563 The instrumental setup of the single-molecule total internal reflection fluorescence (smTIRF) microscope has

564 been previously described⁷³. The DNA constructs designed for the smFRET DNA cyclization assay are detailed
565 in Supplementary Table 1. Single-stranded DNA labeled with fluorophores and biotin was purchased from
566 Integrated DNA Technologies (IDT). For annealing, complementary single-stranded DNAs were resuspended in
567 nuclease-free duplex buffer (IDT), mixed at a 1:1 molar ratio, heated to 95°C for 2 minutes, and then cooled to
568 25°C for over an hour. Polyethylene glycol (PEG)-passivated quartz slides were prepared and assembled
569 according to established protocols⁷⁴. For smTIRF imaging, biotin-labeled DNA oligos were diluted to 50 pM in
570 T10 buffer (10 mM Tris-HCl (pH 8.0), 10 mM NaCl) and heated at 55 °C for 5 minutes to prevent premature
571 annealing via sticky ends before immobilizing on the quartz slide. The DNA was immobilized on the quartz slides
572 through biotin-neutravidin interaction and subsequently washed with T10 buffer after a 2-minute incubation.

573 In the real-time cyclization assay (Fig. 4d), a salt-free imaging buffer (100 mM Tris-HCl (pH 8.0), saturated Trolox,
574 8 mg/ml Dextrose, 0.83 mg/ml glucose oxidase, and 20 U/ml catalase) was introduced to keep the DNA oligos
575 unlooped prior to imaging. For the real-time cyclization experiments, a high-salt imaging buffer (100 mM Tris-
576 HCl (pH 8.0), 1 M NaCl, saturated Trolox, 8 mg/ml Dextrose, 0.83 mg/ml glucose oxidase, and 20 U/ml catalase)
577 was flowed into the channel by a syringe pump. At designated time points, a 20-frame short movie was recorded
578 (10 frames of green excitation, 10 frames of red excitation, 100 ms exposure time). If the imaging time point
579 exceeded 30 minutes after the imaging buffer was flowed into the channel, fresh imaging buffer with the identical
580 salt concentration was introduced into the channel to avoid low pH conditions caused by the oxygen scavenging
581 system. The movies were analyzed using smCamera software^{73,75}, selecting molecules with both green and red
582 emissions for plotting the FRET efficiency histograms. For each time point, ~1000 molecules were used to plot
583 the FRET histogram. The fraction of unlooped and looped DNA oligos were quantified by fitting Gaussian
584 distributions to the low and high FRET peaks using OriginLab software.

585 For measuring protein-induced DNA cyclization (Fig. 4g), the low C0_{corr} DNA (Supplementary Table 1) was
586 immobilized on the quartz slide using the same protocol described above. The protein binding imaging buffer
587 used was 20 mM Tris (pH 7.5), 150 mM NaCl, 1.5 mM MgCl₂, 0.5 mg/ml BSA, saturated Trolox, 8 mg/ml
588 Dextrose, 0.83 mg/ml glucose oxidase, and 20 U/ml catalase. The low C0_{corr} DNA was equilibrated in the protein
589 binding buffer in the channel for 30 minutes, and short movies were recorded to confirm the initial FRET
590 distribution in the absence of proteins. The desired protein was diluted to approximately 60 nM in the protein
591 binding imaging buffer and flowed into the channel using a syringe pump. A series of 20-frame short movies were
592 recorded at designated time points. Data analysis and looping kinetics were conducted in the same manner as
593 described above. All single-molecule measurements were performed at room temperature (~22°C).

594

595 AFM Sample Preparation

596 All DNA oligonucleotides with defined cyclizability were purchased from Ansa Biotechnologies, a DNA
597 manufacturer with expertise in producing long repetitive sequences (Supplementary Table 1). A freshly cleaved
598 mica surface was coated with 20 mM MgCl₂ buffer for 5 minutes, followed by two washes with distilled water.
599 DNA samples, incubated in Tris-HCl buffer with 20 mM MgCl₂ and diluted to 0.1 nM, were then deposited onto
600 the freshly cleaved, MgCl₂-coated mica surface. After a 5-minute incubation, samples were rinsed with either
601 distilled water or MgCl₂ buffer and subsequently imaged using high-speed AFM.

602

603 Specification of High-Speed Atomic Force Microscope (HS-AFM)

604 Experiments on DNA cyclizability across different sequences were conducted using a commercial Sample-
605 Scanning High-Speed Atomic Force Microscope (SS-NEX Ando model) from RIBM (Research Institute of
606 Biomolecule Metrology Co., Ltd.). The AFM was operated in tapping mode to minimize interference with the
607 deposited sample, and all samples shown in this paper were imaged in solution. Ultra-Short Cantilevers (USC-
608 F1.2-k0.15-10), specifically designed for high-speed AFM, were employed with a resonance frequency of 1200
609 kHz, a spring constant of 0.15 N/m, and a length of 7 μm. These cantilevers were purchased from NanoAndMore.
610 A wide scanner was used, with scan speeds ranging from 0.05 to 1 frame per second and resolutions set between

611 200 × 200 and 500 × 500 pixels.

612

613 **Image Processing and Analysis**

614 HS-AFM images were viewed and analyzed using Kodec 4.4.7.39 software (Sakashita M, M Imai, N Kodera, D
615 Maruyama, H Watanabe, Y Moriguchi, and T Ando. 2013. Kodec4.4.7.39). All images were processed with an X-
616 Resonance Noise Filter and X lineTilt correction; detailed image correction protocols are described in the
617 literature⁷⁶. Contrast adjustments were applied to enhance structural features in the images. The length and the
618 average curvature of DNA molecules were analyzed using Fiji⁷¹. DNA molecules shorter than 160 nm were
619 excluded from the analysis due to the possibility of incomplete synthesis or digestion.

620

621 **Data availability**

622 All adapter-dependent cyclizability measurements were downloaded from the sequencing data deposited in NCBI
623 Sequence Read Archive under accession number PRJNA667271, and the genomes of 1,011 yeast isolates were
624 obtained from accession number ERP014555. The mitochondrial genomes of *N. karyoxenos*, *H. phaeocysticola*,
625 *A. motanka*, *S. specki*, *L. lanifica*, *R. humris*, *D. ambulator*, and *D. japonicum* were obtained from the NCBI
626 Nucleotide database under accession number MN109419-MN109581, LC114082-LC114083, MN109174-
627 MN109319, MN109336-MN109400, MN108931-MN109016, MN109083-MN109155, MF436742-MF436795,
628 and MN109036-MN108966. Nucleosome occupancy data through chemical cleavage around nucleosome dyads
629 in *S. cerevisiae* was obtained under NCBI Gene Expression Omnibus accession number GSE97290.

630

631 **Code availability**

632 Code is available on GitHub at <https://github.com/codergirl1106/Cyclizability-Prediction-Website>. A web app is
633 available at <https://cyclizability-prediction-website-5vbkhattypl6n29hkxc8q.streamlit.app/>.

634

635 **Acknowledgements**

636 J.P. and T.H. thank Martha L. Bulyk, Luca Marinai, and Xiao Liu for their advice on the applications of the model.
637 J.P. and T.H. thank Yaojun Zhang, Margarita Gordiychuk, Bohao Fang, and Scott V. Edwards for their helpful
638 discussion. J.P. thanks Basilio C. Huaman for his advice on deep-learning models. This work was supported by
639 the National Institutes of Health grants (R35 GM143949 to L.J.M., R35 GM134842 to C.L.A, R35 GM149357 to
640 S.B., R35 GM122569 to T.H.), the Czech Grant Agency (23-06479X to J.L.) and Wellcome Trust Sir Henry Dale
641 Fellowship (211075/Z/18/Z to R.J.W.). S.B. and T.H. are Investigators of the Howard Hughes Medical Institute.

642

643 **Author contributions**

644 J.P. and T.H. designed the research. J.P. performed all aspects of the research and data analysis. J.P. and T.H. wrote
645 the paper. Other authors contributed to the following areas: G.P. obtained microscopy images of *N. karyoxenos*.
646 A.R.P., D.J.H., and J.D.L. conducted single-molecule TIRF experiments and measured the assembly of inner
647 kinetochore. J.H. conducted single-molecule FRET DNA cyclization assay. T-W.L. conducted atomic force
648 microscopy. S.Y. developed the web prediction tool and verified analysis results for protein-DNA complexes
649 collected from RCSB database. B.K.W. developed heuristic methods to accelerate cyclizability predictions. N.A.B.
650 and L.J.M. provided Nhp6A and HMGB1 for DNA cyclization assay. A.B. advised on the analysis of loop-seq
651 datasets. R.J.W. quantified the content of mtDNA in *N. karyoxenos*. A.B., L.J.M., R.J.W., C.L.A., S.B., and J.L.
652 provided helpful scientific discussion and supported scientific collaboration. All authors commented on the

653 manuscript.

654

655 Competing interests

656 The authors declare no competing interests.

657

658 References

659

660

- 661 1. Basu, A., Bobrovnikov, D.G., Cieza, B., Arcon, J.P., Qureshi, Z., Orozco, M. & Ha, T. Deciphering the
662 mechanical code of the genome and epigenome. *Nat Struct Mol Biol* **29**, 1178-1187 (2022).
- 663 2. Segal, E., Fondufe-Mittendorf, Y., Chen, L., Thastrom, A., Field, Y., Moore, I.K., Wang, J.P. & Widom,
664 J. A genomic code for nucleosome positioning. *Nature* **442**, 772-8 (2006).
- 665 3. Shore, D., Langowski, J. & Baldwin, R.L. DNA flexibility studied by covalent closure of short fragments
666 into circles. *Proc Natl Acad Sci U S A* **78**, 4833-7 (1981).
- 667 4. Vafabakhsh, R. & Ha, T. Extreme bendability of DNA less than 100 base pairs long revealed by single-
668 molecule cyclization. *Science* **337**, 1097-101 (2012).
- 669 5. Basu, A., Bobrovnikov, D.G., Qureshi, Z., Kayikcioglu, T., Ngo, T.T.M., Ranjan, A., Eustermann, S.,
670 Cieza, B., Morgan, M.T., Hejna, M., Rube, H.T., Hopfner, K.P., Wolberger, C., Song, J.S. & Ha, T.
671 Measuring DNA mechanics on the genome scale. *Nature* **589**, 462-467 (2021).
- 672 6. Li, K., Carroll, M., Vafabakhsh, R., Wang, X.A. & Wang, J.P. DNACycP: a deep learning tool for DNA
673 cyclizability prediction. *Nucleic Acids Res* **50**, 3142-3154 (2022).
- 674 7. Khan, S.R., Sakib, S., Rahman, M.S. & Samee, M.A.H. DeepBend: An interpretable model of DNA
675 bendability. *iScience* **26**, 105945 (2023).
- 676 8. Jiang, W.J., Hu, C., Lai, F., Pang, W., Yi, X., Xu, Q., Wang, H., Zhou, J., Zhu, H., Zhong, C., Kuang, Z.,
677 Fan, R., Shen, J., Zhou, X., Wang, Y.J., Wong, C.C.L., Zheng, X. & Wu, H.J. Assessing base-resolution
678 DNA mechanics on the genome scale. *Nucleic Acids Res* **51**, 9552-9566 (2023).
- 679 9. Back, G. & Walther, D. Predictions of DNA mechanical properties at a genomic scale reveal potentially
680 new functional roles of DNA flexibility. *NAR Genom Bioinform* **5**, lqad097 (2023).
- 681 10. Brogaard, K., Xi, L., Wang, J.P. & Widom, J. A map of nucleosome positions in yeast at base-pair
682 resolution. *Nature* **486**, 496-501 (2012).
- 683 11. Luger, K., Mader, A.W., Richmond, R.K., Sargent, D.F. & Richmond, T.J. Crystal structure of the
684 nucleosome core particle at 2.8 Å resolution. *Nature* **389**, 251-60 (1997).
- 685 12. Schumacher, M.A., den Hengst, C.D., Bush, M.J., Le, T.B.K., Tran, N.T., Chandra, G., Zeng, W., Travis,
686 B., Brennan, R.G. & Buttner, M.J. The MerR-like protein BldC binds DNA direct repeats as cooperative
687 multimers to regulate Streptomyces development. *Nat Commun* **9**, 1139 (2018).
- 688 13. Malecka, K.A., Dheekollu, J., Deakyne, J.S., Wiedmer, A., Ramirez, U.D., Lieberman, P.M. & Messick,
689 T.E. Structural Basis for Cooperative Binding of EBNA1 to the Epstein-Barr Virus Dyad Symmetry
690 Minimal Origin of Replication. *J Virol* **93**(2019).
- 691 14. Ru, H., Mi, W., Zhang, P., Alt, F.W., Schatz, D.G., Liao, M. & Wu, H. DNA melting initiates the RAG
692 catalytic pathway. *Nat Struct Mol Biol* **25**, 732-742 (2018).
- 693 15. Berman, H.M., Westbrook, J., Feng, Z., Gilliland, G., Bhat, T.N., Weissig, H., Shindyalov, I.N. & Bourne,
694 P.E. The Protein Data Bank. *Nucleic Acids Res* **28**, 235-42 (2000).
- 695 16. Chua, E.Y., Vasudevan, D., Davey, G.E., Wu, B. & Davey, C.A. The mechanics behind DNA sequence-
696 dependent properties of the nucleosome. *Nucleic Acids Res* **40**, 6338-52 (2012).
- 697 17. Lowary, P.T. & Widom, J. New DNA sequence rules for high affinity binding to histone octamer and
698 sequence-directed nucleosome positioning. *J Mol Biol* **276**, 19-42 (1998).
- 699 18. Makde, R.D., England, J.R., Yennawar, H.P. & Tan, S. Structure of RCC1 chromatin factor bound to the
700 nucleosome core particle. *Nature* **467**, 562-6 (2010).
- 701 19. Vasudevan, D., Chua, E.Y.D. & Davey, C.A. Crystal structures of nucleosome core particles containing
702 the '601' strong positioning sequence. *J Mol Biol* **403**, 1-10 (2010).
- 703 20. Tan, S. & Davey, C.A. Nucleosome structural studies. *Curr Opin Struct Biol* **21**, 128-36 (2011).
- 704 21. Ngo, T.T., Zhang, Q., Zhou, R., Yodh, J.G. & Ha, T. Asymmetric unwrapping of nucleosomes under

- 705 tension directed by DNA local flexibility. *Cell* **160**, 1135-44 (2015).
- 706 22. Yang, Z. & Bielawski, J.P. Statistical methods for detecting molecular adaptation. *Trends Ecol Evol* **15**,
707 496-503 (2000).
- 708 23. Moses, A.M. Statistical tests for natural selection on regulatory regions based on the strength of
709 transcription factor binding sites. *BMC Evol Biol* **9**, 286 (2009).
- 710 24. Vaishnav, E.D., de Boer, C.G., Molinet, J., Yassour, M., Fan, L., Adiconis, X., Thompson, D.A., Levin,
711 J.Z., Cubillos, F.A. & Regev, A. The evolution, evolvability and engineering of gene regulatory DNA.
712 *Nature* **603**, 455-463 (2022).
- 713 25. Peter, J., De Chiara, M., Friedrich, A., Yue, J.X., Pflieger, D., Bergstrom, A., Sigwalt, A., Barre, B., Freel,
714 K., Llored, A., Cruaud, C., Labadie, K., Aury, J.M., Istance, B., Lebrigand, K., Barbry, P., Engelen, S.,
715 Lemainque, A., Wincker, P., Liti, G. & Schacherer, J. Genome evolution across 1,011 *Saccharomyces*
716 *cerevisiae* isolates. *Nature* **556**, 339-344 (2018).
- 717 26. Clarke, L. & Carbon, J. The structure and function of yeast centromeres. *Annu Rev Genet* **19**, 29-55
718 (1985).
- 719 27. Cleveland, D.W., Mao, Y. & Sullivan, K.F. Centromeres and kinetochores: from epigenetics to mitotic
720 checkpoint signaling. *Cell* **112**, 407-21 (2003).
- 721 28. McAinsh, A.D. & Marston, A.L. The Four Causes: The Functional Architecture of Centromeres and
722 Kinetochores. *Annu Rev Genet* **56**, 279-314 (2022).
- 723 29. Santaguida, S. & Musacchio, A. The life and miracles of kinetochores. *EMBO J* **28**, 2511-31 (2009).
- 724 30. Biggins, S. The composition, functions, and regulation of the budding yeast kinetochore. *Genetics* **194**,
725 817-46 (2013).
- 726 31. Bram, R.J. & Kornberg, R.D. Isolation of a *Saccharomyces cerevisiae* centromere DNA-binding protein,
727 its human homolog, and its possible role as a transcription factor. *Mol Cell Biol* **7**, 403-9 (1987).
- 728 32. Meraldi, P., McAinsh, A.D., Rheinbay, E. & Sorger, P.K. Phylogenetic and structural analysis of
729 centromeric DNA and kinetochore proteins. *Genome Biol* **7**, R23 (2006).
- 730 33. Lechner, J. & Carbon, J. A 240 kd multisubunit protein complex, CBF3, is a major component of the
731 budding yeast centromere. *Cell* **64**, 717-25 (1991).
- 732 34. Baker, R.E. & Rogers, K. Genetic and genomic analysis of the AT-rich centromere DNA element II of
733 *Saccharomyces cerevisiae*. *Genetics* **171**, 1463-75 (2005).
- 734 35. Popchock, A.R., Larson, J.D., Dubrulle, J., Asbury, C.L. & Biggins, S. Direct observation of coordinated
735 assembly of individual native centromeric nucleosomes. *EMBO J* **42**, e114534 (2023).
- 736 36. Dechassa, M.L., Wyns, K., Li, M., Hall, M.A., Wang, M.D. & Luger, K. Structure and Scm3-mediated
737 assembly of budding yeast centromeric nucleosomes. *Nat Commun* **2**, 313 (2011).
- 738 37. Dendooven, T., Zhang, Z., Yang, J., McLaughlin, S.H., Schwab, J., Scheres, S.H.W., Yatskevich, S. &
739 Barford, D. Cryo-EM structure of the complete inner kinetochore of the budding yeast point centromere.
740 *Sci Adv* **9**, eadg7480 (2023).
- 741 38. Gillespie, J.H. Molecular Evolution over the Mutational Landscape. *Evolution* **38**, 1116-1129 (1984).
- 742 39. Anishchenko, I., Pellock, S.J., Chidyausiku, T.M., Ramelot, T.A., Ovchinnikov, S., Hao, J., Bafna, K.,
743 Norn, C., Kang, A., Bera, A.K., DiMaio, F., Carter, L., Chow, C.M., Montelione, G.T. & Baker, D. De
744 novo protein design by deep network hallucination. *Nature* **600**, 547-552 (2021).
- 745 40. Crothers, D.M., Haran, T.E. & Nadeau, J.G. Intrinsically bent DNA. *J Biol Chem* **265**, 7093-6 (1990).
- 746 41. Koo, H.S., Wu, H.M. & Crothers, D.M. DNA bending at adenine . thymine tracts. *Nature* **320**, 501-6
747 (1986).
- 748 42. Hagerman, P.J. Sequence dependence of the curvature of DNA: a test of the phasing hypothesis.
749 *Biochemistry* **24**, 7033-7 (1985).
- 750 43. Thomas, J.O. & Travers, A.A. HMG1 and 2, and related 'architectural' DNA-binding proteins. *Trends
751 Biochem Sci* **26**, 167-74 (2001).
- 752 44. Travers, A.A. Priming the nucleosome: a role for HMGB proteins? *EMBO Rep* **4**, 131-6 (2003).
- 753 45. Altschul, S.F., Gish, W., Miller, W., Myers, E.W. & Lipman, D.J. Basic local alignment search tool. *J
754 Mol Biol* **215**, 403-10 (1990).
- 755 46. Kaur, B., Zahonova, K., Valach, M., Faktorova, D., Prokopchuk, G., Burger, G. & Lukes, J. Gene
756 fragmentation and RNA editing without borders: eccentric mitochondrial genomes of diplomonads.
757 *Nucleic Acids Res* **48**, 2694-2708 (2020).
- 758 47. Valach, M., Moreira, S., Petitjean, C., Benz, C., Butenko, A., Flegontova, O., Nenarokova, A.,
759 Prokopchuk, G., Batstone, T., Lapebie, P., Lemogo, L., Sarrasin, M., Stretenowich, P., Tripathi, P., Yazaki,
760 E., Nara, T., Henrissat, B., Lang, B.F., Gray, M.W., Williams, T.A., Lukes, J. & Burger, G. Recent
761 expansion of metabolic versatility in *Diplonema papillatum*, the model species of a highly speciose group
762 of marine eukaryotes. *BMC Biol* **21**, 99 (2023).
- 763 48. Lukes, J., Wheeler, R., Jirsova, D., David, V. & Archibald, J.M. Massive mitochondrial DNA content in

- 764 diplonemid and kinetoplastid protists. *IUBMB Life* **70**, 1267-1274 (2018).
- 765 49. Satoh, M. & Kuroiwa, T. Organization of multiple nucleoids and DNA molecules in mitochondria of a
766 human cell. *Exp Cell Res* **196**, 137-40 (1991).
- 767 50. Bogenhagen, D.F., Rousseau, D. & Burke, S. The layered structure of human mitochondrial DNA
768 nucleoids. *J Biol Chem* **283**, 3665-3675 (2008).
- 769 51. Hensen, F., Cansiz, S., Gerhold, J.M. & Spelbrink, J.N. To be or not to be a nucleoid protein: a
770 comparison of mass-spectrometry based approaches in the identification of potential mtDNA-nucleoid
771 associated proteins. *Biochimie* **100**, 219-26 (2014).
- 772 52. Brewer, L.R., Friddle, R., Noy, A., Baldwin, E., Martin, S.S., Corzett, M., Balhorn, R. & Baskin, R.J.
773 Packaging of single DNA molecules by the yeast mitochondrial protein Abf2p. *Biophys J* **85**, 2519-24
774 (2003).
- 775 53. Gustafsson, C.M., Falkenberg, M. & Larsson, N.G. Maintenance and Expression of Mammalian
776 Mitochondrial DNA. *Annu Rev Biochem* **85**, 133-60 (2016).
- 777 54. Butenko, A., Opperdoes, F.R., Flegontova, O., Horak, A., Hampl, V., Keeling, P., Gawryluk, R.M.R.,
778 Tikhonenkov, D., Flegontov, P. & Lukes, J. Evolution of metabolic capabilities and molecular features
779 of diplonemids, kinetoplastids, and euglenids. *BMC Biol* **18**, 23 (2020).
- 780 55. Jensen, R.E. & Englund, P.T. Network news: the replication of kinetoplast DNA. *Annu Rev Microbiol* **66**,
781 473-91 (2012).
- 782 56. Prokophchuk, G., Tashyreve, D., Yabuki, A., Horak, A., Masarova, P. & Lukes, J. Morphological,
783 Ultrastructural, Motility and Evolutionary Characterization of Two New Hemistasiidae Species. *Protist*
784 **170**, 259-282 (2019).
- 785 57. Wu, R. & Li, H. Positioned and G/C-capped poly(dA:dT) tracts associate with the centers of nucleosome-
786 free regions in yeast promoters. *Genome Res* **20**, 473-84 (2010).
- 787 58. Li, N., Lam, W.H., Zhai, Y., Cheng, J., Cheng, E., Zhao, Y., Gao, N. & Tye, B.K. Structure of the origin
788 recognition complex bound to DNA replication origin. *Nature* **559**, 217-222 (2018).
- 789 59. Marini, J.C., Levene, S.D., Crothers, D.M. & Englund, P.T. Bent helical structure in kinetoplast DNA.
790 *Proc Natl Acad Sci U S A* **79**, 7664-8 (1982).
- 791 60. Burkhoff, A.M. & Tullius, T.D. The unusual conformation adopted by the adenine tracts in kinetoplast
792 DNA. *Cell* **48**, 935-43 (1987).
- 793 61. Sutormin, D., Rubanova, N., Logacheva, M., Ghilarov, D. & Severinov, K. Single-nucleotide-resolution
794 mapping of DNA gyrase cleavage sites across the Escherichia coli genome. *Nucleic Acids Res* **47**, 1373-
795 1388 (2019).
- 796 62. Chakraborty, A., Lyonnais, S., Battistini, F., Hospital, A., Medici, G., Prohens, R., Orozco, M., Vilardell,
797 J. & Sola, M. DNA structure directs positioning of the mitochondrial genome packaging protein Abf2p.
798 *Nucleic Acids Res* **45**, 951-967 (2017).
- 799 63. Farge, G. & Falkenberg, M. Organization of DNA in Mammalian Mitochondria. *Int J Mol Sci* **20**(2019).
- 800 64. Chollet, F. keras, (2015).
- 801 65. Kingma, D.P. Adam: A method for stochastic optimization. *arXiv preprint arXiv:1412.6980* (2014).
- 802 66. Virtanen, P., Gommers, R., Oliphant, T.E., Haberland, M., Reddy, T., Cournapeau, D., Burovski, E.,
803 Peterson, P., Weckesser, W., Bright, J., van der Walt, S.J., Brett, M., Wilson, J., Millman, K.J., Mayorov,
804 N., Nelson, A.R.J., Jones, E., Kern, R., Larson, E., Carey, C.J., Polat, I., Feng, Y., Moore, E.W.,
805 VanderPlas, J., Laxalde, D., Perktold, J., Cimrman, R., Henriksen, I., Quintero, E.A., Harris, C.R.,
806 Archibald, A.M., Ribeiro, A.H., Pedregosa, F., van Mulbregt, P. & SciPy, C. SciPy 1.0: fundamental
807 algorithms for scientific computing in Python. *Nat Methods* **17**, 261-272 (2020).
- 808 67. Kent, W.J. BLAT--the BLAST-like alignment tool. *Genome Res* **12**, 656-64 (2002).
- 809 68. Cherry, J.M., Hong, E.L., Amundsen, C., Balakrishnan, R., Binkley, G., Chan, E.T., Christie, K.R.,
810 Costanzo, M.C., Dwight, S.S., Engel, S.R., Fisk, D.G., Hirschman, J.E., Hitz, B.C., Karra, K., Krieger,
811 C.J., Miyasato, S.R., Nash, R.S., Park, J., Skrzypek, M.S., Simison, M., Weng, S. & Wong, E.D.
812 Saccharomyces Genome Database: the genomics resource of budding yeast. *Nucleic Acids Res* **40**, D700-
813 5 (2012).
- 814 69. Drew, H.R., Wing, R.M., Takano, T., Broka, C., Tanaka, S., Itakura, K. & Dickerson, R.E. Structure of a
815 B-DNA dodecamer: conformation and dynamics. *Proc Natl Acad Sci U S A* **78**, 2179-83 (1981).
- 816 70. Aitken, C.E., Marshall, R.A. & Puglisi, J.D. An oxygen scavenging system for improvement of dye
817 stability in single-molecule fluorescence experiments. *Biophys J* **94**, 1826-35 (2008).
- 818 71. Schindelin, J., Arganda-Carreras, I., Frise, E., Kaynig, V., Longair, M., Pietzsch, T., Preibisch, S., Rueden,
819 C., Saalfeld, S., Schmid, B., Tinevez, J.Y., White, D.J., Hartenstein, V., Eliceiri, K., Tomancak, P. &
820 Cardona, A. Fiji: an open-source platform for biological-image analysis. *Nat Methods* **9**, 676-82 (2012).
- 821 72. Yurchenko, V., Votypka, J., Tesarova, M., Klepetkova, H., Kraeva, N., Jirku, M. & Lukes, J.
822 Ultrastructure and molecular phylogeny of four new species of monoxenous trypanosomatids from flies

- 823 (Diptera: Brachycera) with redefinition of the genus Wallaceina. *Folia Parasitol (Praha)* **61**, 97-112
 824 (2014).

825 73. Roy, R., Hohng, S. & Ha, T. A practical guide to single-molecule FRET. *Nat Methods* **5**, 507-16 (2008).

826 74. Paul, T. & Myong, S. Protocol for generation and regeneration of PEG-passivated slides for single-
 827 molecule measurements. *STAR Protoc* **3**, 101152 (2022).

828 75. Lee, K.S. & Ha, T. smCamera: all-in-one software package for single-molecule data acquisition and data
 829 analysis. *Journal of the Korean Physical Society* (2024).

830 76. Ngo, K.X., Kodera, N., Katayama, E., Ando, T. & Uyeda, T.Q. Cofilin-induced unidirectional
 831 cooperative conformational changes in actin filaments revealed by high-speed atomic force microscopy.
 832 *Elife* **4**(2015).

833 77. Brogaard, K.R., Xi, L., Wang, J.P. & Widom, J. A chemical approach to mapping nucleosomes at base
 834 pair resolution in yeast. *Methods Enzymol* **513**, 315-34 (2012).

835 78. Tashyreva, D., Simpson, A.G.B., Prokopchuk, G., Skodova-Sverakova, I., Butenko, A., Hammond, M.,
 836 George, E.E., Flegontova, O., Zahonova, K., Faktorova, D., Yabuki, A., Horak, A., Keeling, P.J. & Lukes,
 837 J. Diplonemids - A Review on "New" Flagellates on the Oceanic Block. *Protist* **173**, 125868 (2022).

838 79. Bailey, T.L. & Elkan, C. Fitting a mixture model by expectation maximization to discover motifs in
 839 biopolymers. *Proc Int Conf Intell Syst Mol Biol* **2**, 28-36 (1994).

840

841

842

843 **Fig. 1**

844 **Highly accurate prediction of cyclizability.**

845 **a**, Schematic of loop-seq and cyclizability measurement (adopted from Basu et al⁵). **b**, Schematic of the model
846 training process and scatter plot showing measured vs predicted C0 for the training dataset from the Tiling library⁵.
847 A detailed schematic is found in Supplementary Fig. 3b. For model performance on the testing datasets, see
848 Supplementary Fig. 4a. Pearson's correlation, sample size, and the corresponding two-tailed *P*-value are shown.
849 **c**, Performance of our prediction on the ChrV dataset (red) relative to previous predictions^{1,6-9} (gray). Error bar is
850 a 95% confidence interval of Pearson's correlation coefficient *R*. **d**, Schematic of adapter-dependent (C0) and
851 adapter-corrected (C0_{corr}) cyclizability. **e**, C0 values of the original vs the reverse complementary sequence of
852 Tiling library. **f**, C0_{corr} of the original vs the reverse complementary sequence of Tiling library. **e, f**, Pearson's
853 correlation coefficient *R*, sample size, and the related two-tailed *P*-value are shown.

854

855 **Fig. 2**

856 **Selection of DNA mechanical properties in available structures.**

857 **a**, Cyclization rate is affected by anisotropic DNA bending in space. **b**, DNA bending of yeast nucleosome DNA
858 with top or bottom 10% score-to-noise ratio for the dyad positions inferred from chemical mapping data^{10,77}. The
859 magnitude of predicted bending as denoted as red lines was scaled by a factor of 100 when visualized in 3-
860 dimensional space (Methods). **c, d, e**, 3-dimensional DNA bending of protein-DNA complexes overlaid with the
861 original structures. PDB IDs 6AMA, 6PW2, and 6DBT were used, respectively. **f**, Bending of original DNA
862 sequences used in the reported structures in protein data bank (PDB) vs randomized sequences in 3-dimensional
863 space. The predicted direction of DNA bending is shown in red, and the line length is proportional to the magnitude
864 of bending predicted (Methods). **g**, Similarity score is an inner product of vectors for intrinsic bending and
865 observed bending (Methods). Selection of DNA mechanical properties for all (**h**), as well as for the most bent (top
866 10%) and the least bent (bottom 10%) DNA molecules (**i**), within the curated set of protein-DNA structures in
867 RCSB database. Mechanical properties were evaluated using a normalized similarity score, which is similarity
868 divided by DNA bending vector length (Methods). **j**, Similarity score averaged over each DNA in the published
869 nucleosome structures vs publication year. Black symbols are for nucleosome structures whose sequence could
870 not be assigned to one of the annotated sequences denoted by colored symbols. **k**, Similarity score averaged over
871 each nucleosome DNA vs salt stability measured in Chua et al¹⁶.

872

873 **Fig. 3**

874 **Mechanical selection in yeast centromeres modulates the stability of inner kinetochores.**

875 **a**, Schematic of the process quantifying mechanical selection using the populational genetics data of yeast²⁵ (Methods).
876 **b**, Cyclizability and mechanical selection (Z-score) averaged over 16 yeast centromeres collected from 1,011 yeast
877 isolates. Regions of negative Z-score are highlighted blue. **c**, Mechanical selection in CEN2, 3, 5, and 13. Pro-
878 and anti-rigidity selection are marked by red and blue colors, respectively (Methods). **d**, Intrinsic propensity of
879 DNA bending (top) and mechanical selection (bottom) in inner kinetochore. The results are overlaid on the 3-
880 dimensional structure of inner kinetochore (PDB 8OW1, left), and the corresponding similarity scores are plotted
881 (right). **e**, Schematic of the fluorescent label location used in smTIRF colocalization assay. **f**, Overview of sacCer3,
882 natural, and cyclizability-changing CDEII DNA mutants used for single molecule fluorescence colocalization
883 analysis. **g**, Cyclizability of CDEII sequences in **f**. **h**, Example images of total internal reflection fluorescent
884 microscopy endpoint colocalization analysis of visualized Cse4-GFP on sacCer3 CDEII DNA (left), CDEII with
885 natural mutations (middle) or cyclizability-changing mutations (right), with colocalization shown in relation to
886 identified DNA in blue circles. Bottom panels show respective overlays of DNA channel (magenta) with Cse4-
887 GFP (green). Scale bars: 3 μ m. **i**, Graph indicates quantification of endpoint colocalization of Cse4 on CDEII
888 DNA (left), CDEII with natural mutations (middle) and cyclizability-changing mutations (left). Points indicate
889 individual experiments (n=3) where ~1,000 DNA molecules were identified per replicate.

890

891 **Fig. 4**

892 **Evolution of extreme cyclizability in *Namystinia karyoxenos* mitochondrial DNA.**

893 **a**, Schematic of *in silico* evolution. Starting with 6,420 random 50 bp sequences, 150 point mutations are generated
894 from each sequence. The mutation that finds the extrema of $C_{0\text{corr}}$ (directional selection) or a random mutation
895 (genetic drift) is selected as the input for the next round. **b**, Change in $C_{0\text{corr}}$ relative to the starting sequence after
896 0, 1, 2, 4, 8, 16, and 32 mutational steps of genetic drift, starting with 6,420 random 50 bp sequences. Differences
897 between the $C_{0\text{corr}}$ of random 50 bp sequences and arbitrarily assigned starting sequences were plotted separately
898 as an unrelated set. **c**, $C_{0\text{corr}}$ after the indicated number of mutational steps of directional selection, starting from
899 6,420 random 50 bp sequences. Gray, $C_{0\text{corr}}$ in yeast chromosome V, red, maximizing selection, blue, minimizing
900 selection. **b**, **c**, Whisker box plots are shown together with the scattered data. **d**, The fraction of looped DNA
901 molecules in the real-time single-molecule cyclization assay (Methods). 50 bp DNA sequences with extremely
902 high ($C_{0\text{corr}} \sim 3.055$) or low cyclizability ($C_{0\text{corr}} \sim -2.202$) were used. Error bars are standard deviations of three
903 experiments. **e**, Example AFM images of a 600 bp linear segment of mitochondrial DNA of *N. karyoxenos* and
904 two DNA molecules of the same length with extremely high or low cyclizability (Methods). Cyclizability vs
905 position for the 600 bp DNA sequences is shown in Supplementary Fig. 9e. The top row shows the whole field
906 (scale bar: 200 nm), and the bottom rows show zoom-ins (scale bar: 40 nm). **f**, Static curvature averaged per DNA
907 molecule in AFM images (Methods). *P*-values (two-tailed t-test) lower than 0.05 are indicated as *. **g**, The fraction
908 of looped DNA molecules in the real-time single-molecule cyclization assay after the addition of DNA-bending
909 proteins (Methods). DNA with low cyclizability used in the previous cyclization assay in **d** was tested with the
910 addition of Nhp6A (n=3 experiments) and HMGB1 (n=1 experiment). Error bars represent standard deviations of
911 replicates. **h**, Cladogram depicting the phylogenetic relationships of diplomonad protists⁷⁸ and the average $C_{0\text{corr}}$
912 in non-coding regions of mitochondrial genomes. Classes of mitochondrial genomes are noted next to species
913 names. **i**, Transmission electron micrographs of *N. karyoxenos* displaying reticulated peripheral mitochondrial
914 branches (arrows, left panel) and bead-like electron-dense mtDNA (arrowheads) located among the mitochondrial
915 cristae (right panel). Scale bar: 1 μm. **j**, Light microscopy micrographs of *N. karyoxenos* labelled with the minor
916 groove binder, Hoechst 33342, as well as with the base pair intercalating dye, PI. DIC - differential interference
917 contrast. Scale bar: 1 μm. **k**, Proportion of nuclear and non-nuclear (mitochondrial and endosymbiont) DNA as
918 measured from PI fluorescence signal. $n = 372$ cells, error bars represent standard error of proportion. **l**,
919 Cyclizability along chromosome 39 of *H. mexicanus*. **m**, Average cyclizability vs length of each chromosome of
920 *H. mexicanus*. Spearman's *R* and the related two-tailed *P*-value are shown. **n**, Spearman's *R* between average
921 cyclizability vs length of each chromosome for 60 different bird species and four non-bird neighbors. Error bars
922 indicate 95% CI.

923

924 **Supplementary Fig. 1**

925 **Schematic of a typical DNA molecule in loop-seq.**

926 DNA molecule for loop-seq consists of a variable region (50 bp) surrounded by two adapters (25 bp each) and 5'
927 ssDNA overhangs (10 nt). The ssDNA overhangs are complementary to each other and form dsDNA after looping⁵.
928 DNA looping (or cyclization) reaction rate depends on biotin position for sequences that induce static bending,
929 and the biotin position dependence of cyclizability can be eliminated by performing loop-seq with three different
930 biotin positions indicated yielding C26, C29 and C31, and mathematically correcting for the position effect
931 (Methods).

932

933 **Supplementary Fig. 2**

934 **Read counts are anti-correlated with the 95% CI of measured cyclizability.**

935 **a**, Read counts vs measured cyclizability distribution. Lower read counts would give rise to a broader distribution
936 because relative errors are larger. **b**, Distribution of read counts in loop-seq experiments measuring C26 in the
937 Random, Tiling, and ChrV library. **c**, Total read count (before + after digestion) of each sequence vs the
938 corresponding 95% CI of measured C26 in Random, Tiling, and ChrV library. **d**, Distribution of the 95% CI of

939 C26 in the Random, Tiling, and ChrV library. **e**, Scatter plots of repeated C26 measurements on the Cerevisiae
940 Nucleosome library. Top 20, 50, 100, 250, 1,000, 2,500, 10,000, 19,638 sequences with the lowest sum of 95%
941 CI of repeated measurements were selected. Sample sizes and Pearson's correlations are shown. Measurement 1
942 is from loop-seq of the mixture of Random and Cerevisiae Nucleosome library. Measurement 2 is from the 1-
943 minute time point of the timecourse loop-seq on the Cerevisiae Nucleosome library.

944

945 **Supplementary Fig. 3**

946 **Training model to predict cyclizability.**

947 **a**, Model structure for learning cyclizability. **b**, Schematic of the model training process and scatter plot showing
948 measured vs predicted C0 for the training dataset curated from the Tiling library⁵. Pearson's correlation, sample
949 size, and the corresponding two-tailed P-value are shown. Note that we are showing the same scatter plot as in
950 Fig. 1b in this expanded schematic of model training. **c**, Measured C26, 95% CI, and predictions for an example
951 region of yeast chromosome V.

952

953 **Supplementary Fig. 4**

954 **Prediction accuracy of cyclizability is affected by read counts.**

955 **a**, Measured vs predicted cyclizability of sequences with an uncertainty score below 0.1 in the ChrV library. **b**,
956 Repeated measurements of C26 for the Cerevisiae Nucleosome library compared to predictions. For each
957 sequence, the C26 measurement with the narrower 95% CI is used in the left plot (Pearson's $R = 0.906$), while the
958 measurement with the wider 95% CI is used in the right plot (Pearson's $R = 0.860$). C26 measurements with
959 narrower 95% CI show a stronger correlation with the predicted C26 ($P < 10^{-98}$). For the repeated measurements,
960 the mixture of Random and Cerevisiae Nucleosome library and timecourse loop-seq on Cerevisiae Nucleosome
961 library at 1-minute were compared. **c**, Measured vs predicted C26 in subgroups of the Random and ChrV library.
962 Sequences were sorted and classified into 8 subgroups based on the width of 95% CI of C26.

963

964 **Supplementary Fig. 5**

965 **Defining and learning adapter-corrected cyclizability.**

966 **a**, Schematic of the procedure for defining the corrected upper and lower envelopes, and C0_{corr} (Method). **b**, The
967 relationship between adapter-corrected cyclizability and corrected envelopes. **c**, AT content across 50 bp DNA
968 averaged over 1,000 sequences curated from the Random library with the highest C_{corr} values, red, or the lowest
969 C_{corr} values, blue. **d**, Scatter plots comparing repeated calculations of C_{corr}. Different sets of upstream and
970 downstream 50 bp sequences were used for repeated calculations of C_{corr} (Supplementary Note 4). **e**, C_{corr}
971 calculated from predicted C values vs the corresponding C_{corr} values predicted directly from models that are
972 trained using C_{corr}. **f**, C0_{corr} of 55 bp DNA sequences in the library L vs the corresponding C0_{corr} of 50 bp DNA
973 sequences in the Random library. A set of sequences in the library L and the Random library share the same 50 bp
974 from the 5' end. Details can be found in Supplementary Note 4.

975

976 **Supplementary Fig. 6**

977 **Selection of DNA mechanics in experimentally determined structures**

978 **a**, Selection of DNA mechanics in different molecular types. P-values by the paired t-tests between randomized
979 and original DNA sequences are shown. **b**, **c**, **d**, **e**, DNA mechanical properties of complexes shown in PDB IDs
980 of 1AOI, 3LZ0, 3UT9, and 3UTB, respectively. 3-dimensional DNA bending is overlaid with PDB structures
981 (left), and the corresponding cyclizability and similarity scores are plotted (right).

982

983 **Supplementary Fig. 7**

984 **Colocalization of centromere DNA and Ndc10 in inner kinetochore**

985 **a**, Example images of total internal reflection fluorescent microscopy endpoint colocalization assays of visualized
986 Ndc10-mCherry on sacCer3 CDEII DNA (left), CDEII with natural mutations (middle) or cyclizability-changing
987 mutations (right), with colocalization shown in relation to identified DNA in blue circles. Bottom panels show
988 respective overlays of DNA channel (magenta) with Ndc10-mCherry (yellow). Scale bars: 3 μ m. **b**, Graph
989 indicates quantification of endpoint colocalization of Ndc10 on sacCer3 CDEII DNA (left), CDEII with natural
990 mutations (middle) or cyclizability-changing mutations (left). Points indicate individual experiments (n=3) where
991 ~1,000 DNA molecules were identified per replicate.

992

993 **Supplementary Fig. 8**

994 **Accumulation of poly(dA:dT) tracts during *in silico* evolution.**

995 **a**, The number of bases that belong to a poly(dA:dT), defined as runs of dAs or dTs of the indicated length found
996 in the pool of sequences under maximizing selection (Fig. 4c). **b**, Proportion of matching bases of the same type
997 at each distance after 50 maximizing steps. For example, the sequence 5'-NNANNANN-3' is used to count
998 adenine (A) matches at a distance of 3 bases. **c**, **d**, Repeat of **a** and **b** but for minimizing selection, respectively. **e**,
999 Three sequences with the highest predicted $C_{0,\text{corr}}$ found after 50 steps of maximizing selection. **f**, Repeat of **e** but
1000 for the lowest predicted $C_{0,\text{corr}}$. **g**, Two sequences with the lowest and two sequences with the highest measured
1001 C_0 in the Tiling library. The measured C_0 of adjacent sequences was plotted together. Poly(dA:dT) tracts longer
1002 than 5 bp are highlighted in the dashed boxes. **a**, **c**, **g**, Any continuous fragment of dA, dT, or their mixtures, such
1003 as 5'-ATTATAT-3', is considered a poly(dA:dT) tract.

1004

1005 **Supplementary Fig. 9**

1006 **Extreme DNA mechanics in Hemistasiidae mitochondrial genomes.**

1007 **a**, Top hits from the BLASTn alignment results using the 50 bp DNA with the highest $C_{0,\text{corr}}$ found after the
1008 maximizing selection (the first sequence of Supplementary Fig 8e, Methods). **b**, Mitochondrial genomes of *H.*
1009 *phaeocysticola* found in the same BLASTn search in **a**. **c**, $C_{0,\text{corr}}$ of the four regions of mitochondrial genomes of
1010 *N. karyoxenos* containing unusually high $C_{0,\text{corr}}$. Coding regions are highlighted in the blue shaded areas. **d**, The
1011 repetitive 50 bp motif found in the mitochondrial genomes of *N. karyoxenos*, based on MEME analysis⁷⁹. **e**, $C_{0,\text{corr}}$
1012 vs position for the three 600 bp DNA used in AFM images in Fig. 4e. **f**, Natural mutations in the mitochondrial
1013 repeat motifs rarely show $C_{0,\text{corr}}$ below 2, but random mutations do. The Hamming distance for the native and
1014 random mutations was preserved (Methods).

1015

1016 **Supplementary Fig. 10**

1017 **Micrographs of nucleus and mitochondria of *N. karyoxenos***

1018 **a**, Relative *in vitro* Hoechst 33342 and PI fluorescence intensity when mixed with dsDNA with a range of
1019 cyclizabilities. Fluorescence signal intensity was normalized to the mean of three samples with close zero
1020 cyclizability. Open circles are data points from individual replicates (n = 3), solid circles represent the mean, error
1021 bars represent the standard deviation. **b**, Overlay of z-stack images from confocal microscopy showing combined
1022 immunofluorescence (IF, Alexa488) and fluorescence *in situ* hybridization (FISH, Cy3) analysis. IF assay was
1023 performed using an antibody against the β chain of mitochondrial ATP synthase, FISH using a DNA-Cy3 probe
1024 which labelled circularized mtDNA regions. Dashed lines encircle the nucleus. Scale bar: 1 μ m.

1025

1026 **Supplementary Fig. 11**

1027 **Cyclizability of two example chromosomes**

1028 **a**, Cyclizability along chromosome 30 of *M. undulatus*. **b**, Cyclizability along chromosome 16 of *A. mississippiensis*. **c**, Chromosome size vs average cyclizability per chromosome for 60 bird species and 4 outgroups.
1029
1030 Gray dots indicate the distribution of all chromosomes collected from 60 bird species.

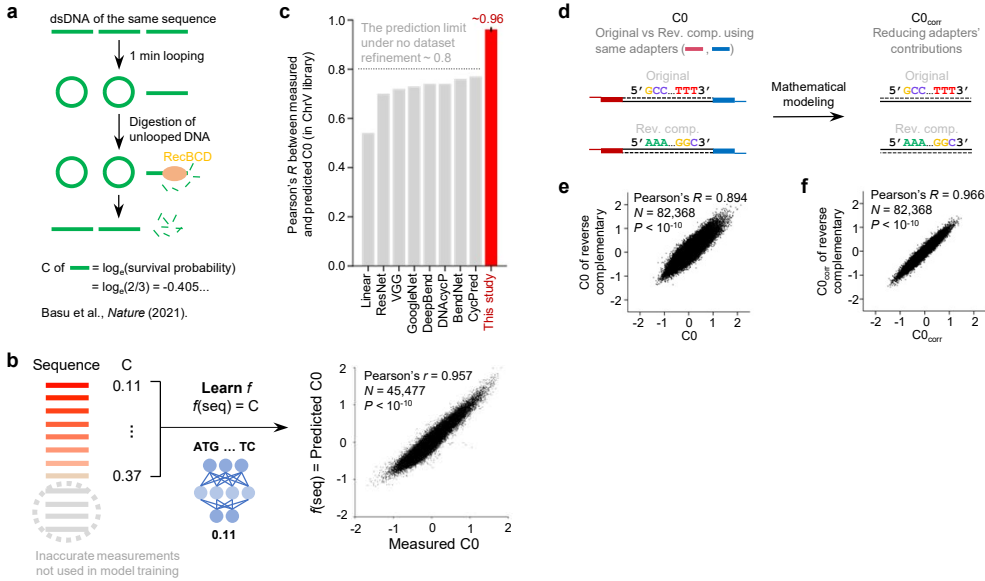


Fig. 1

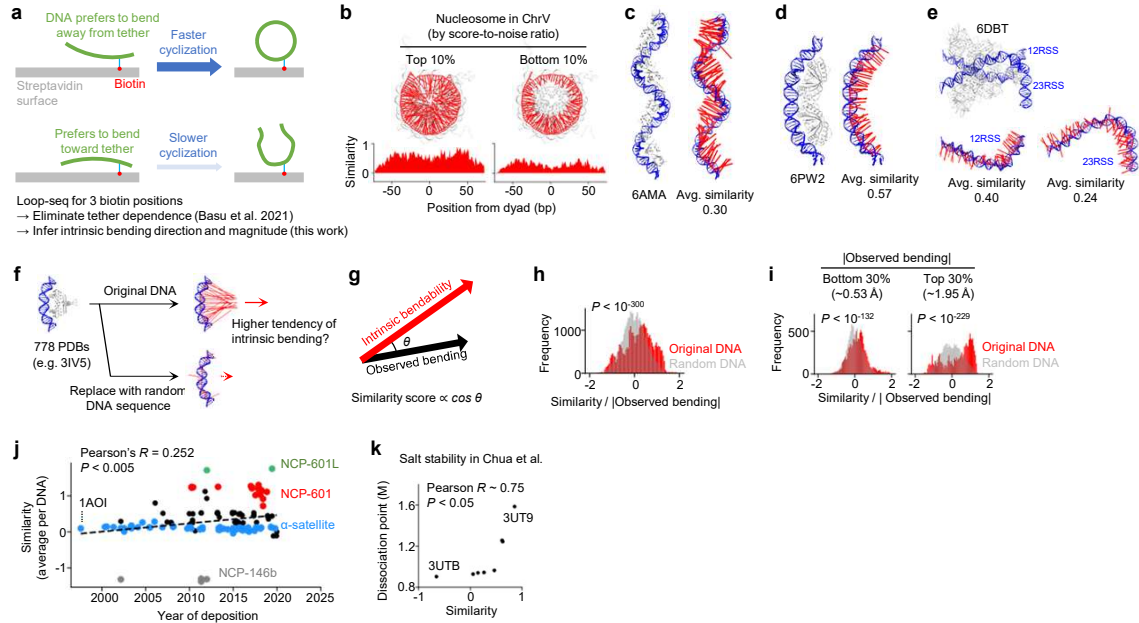


Fig. 2

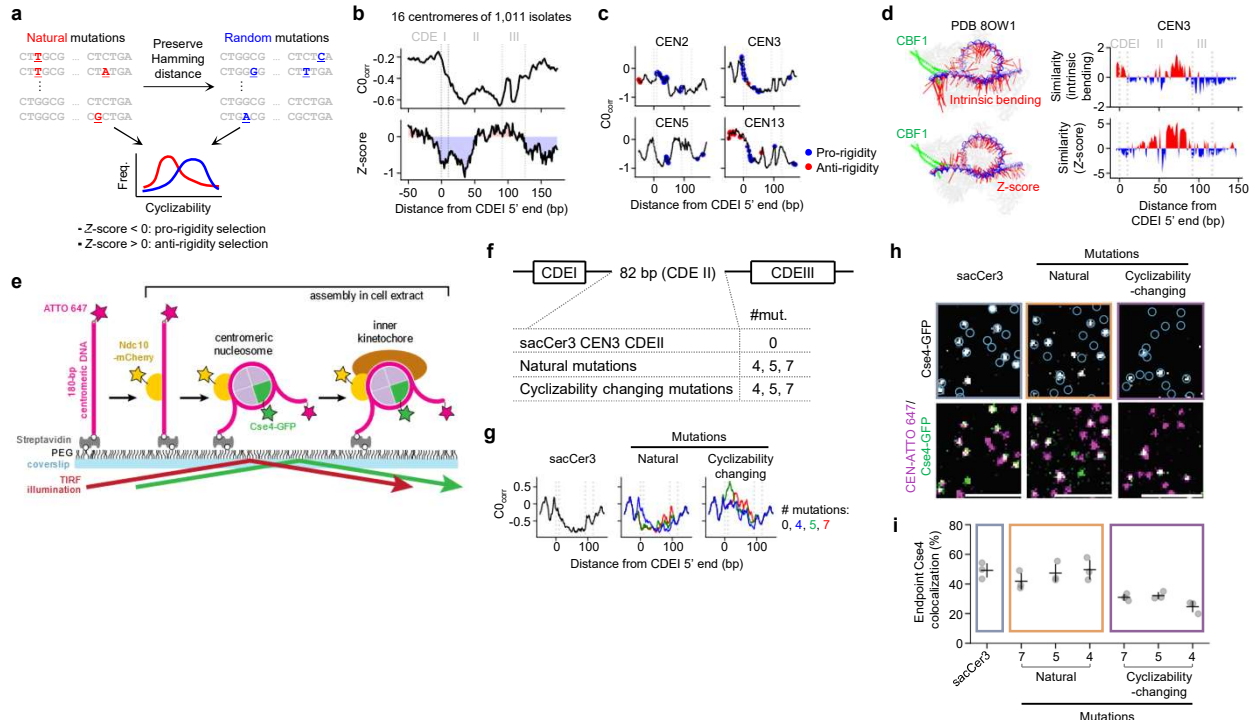


Fig. 3

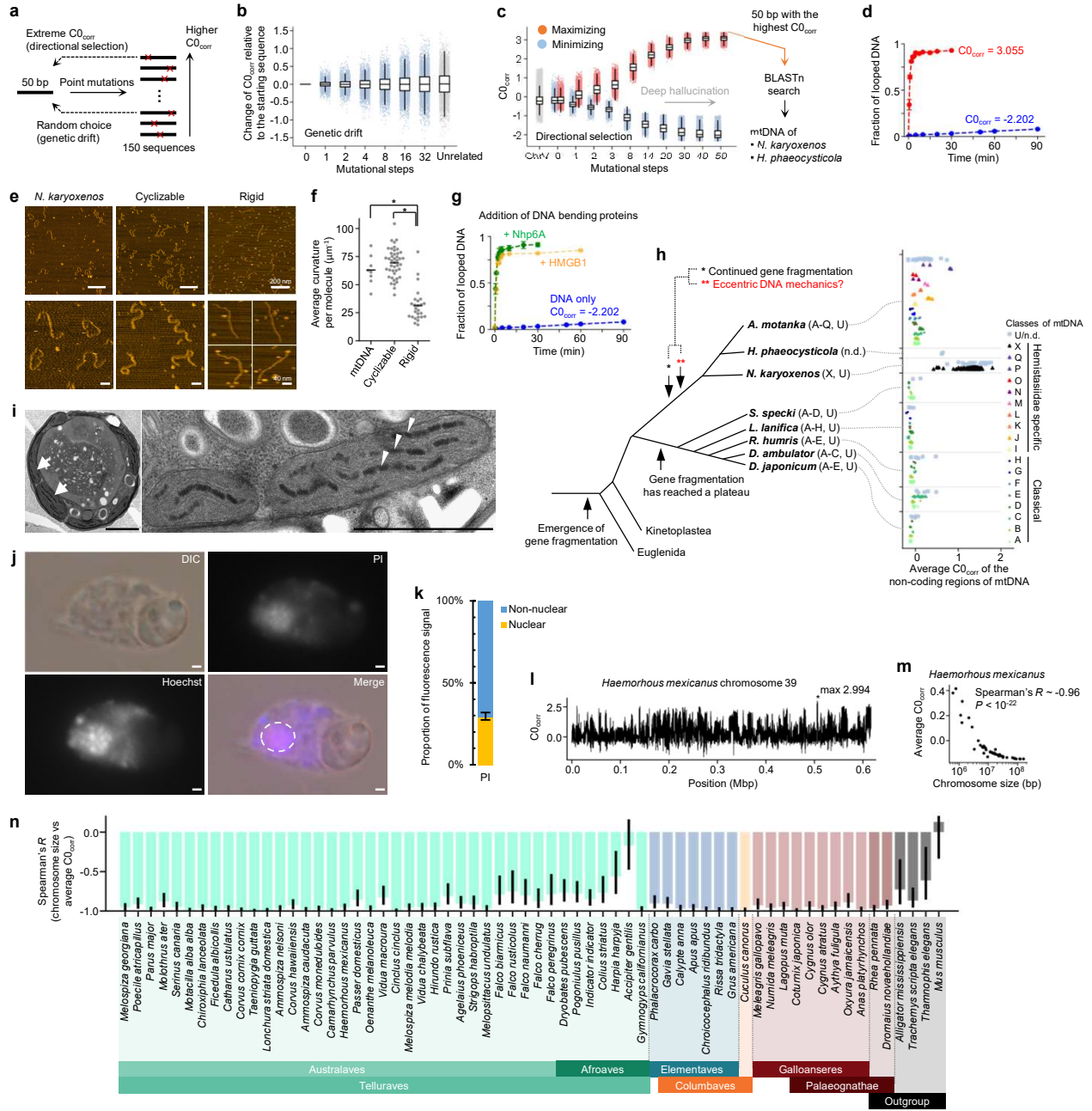
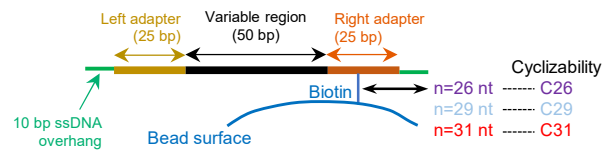
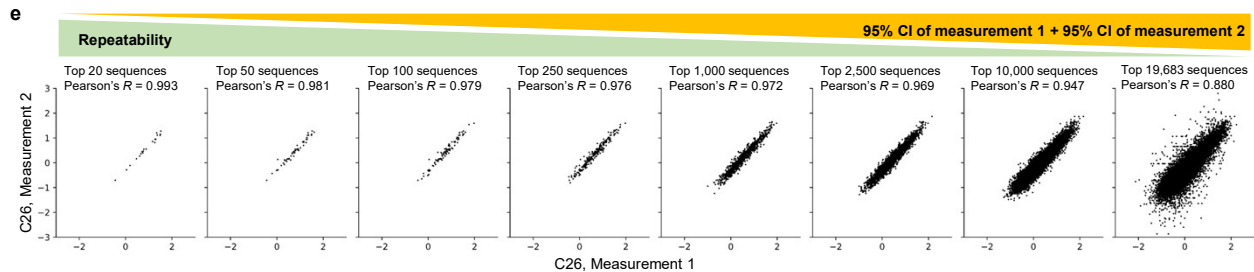
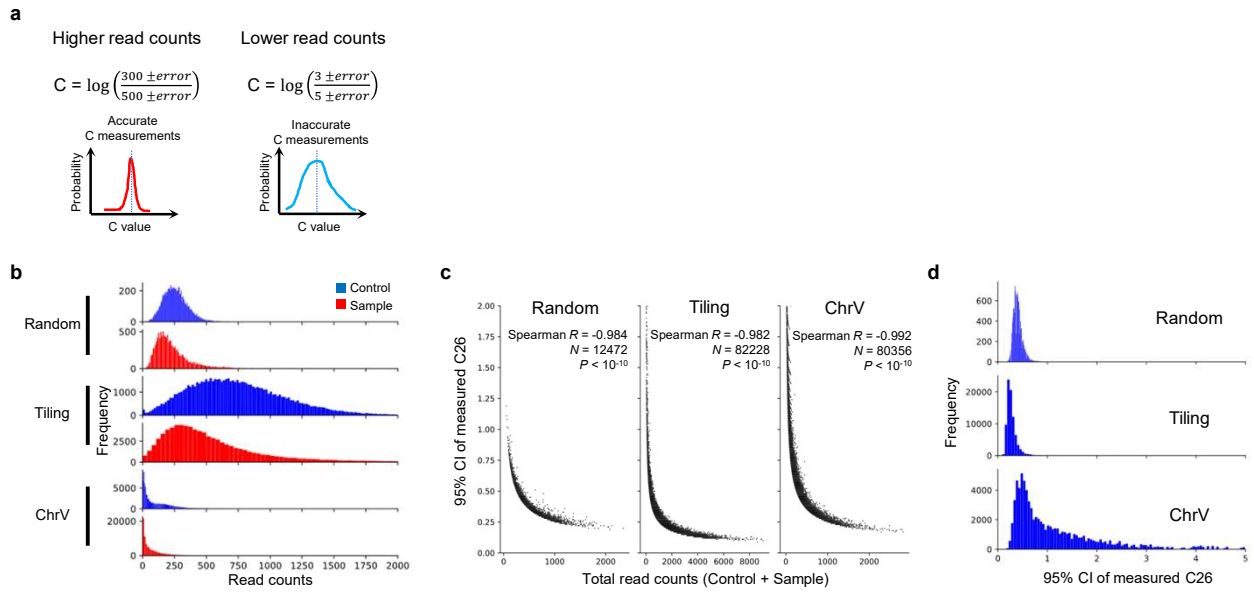


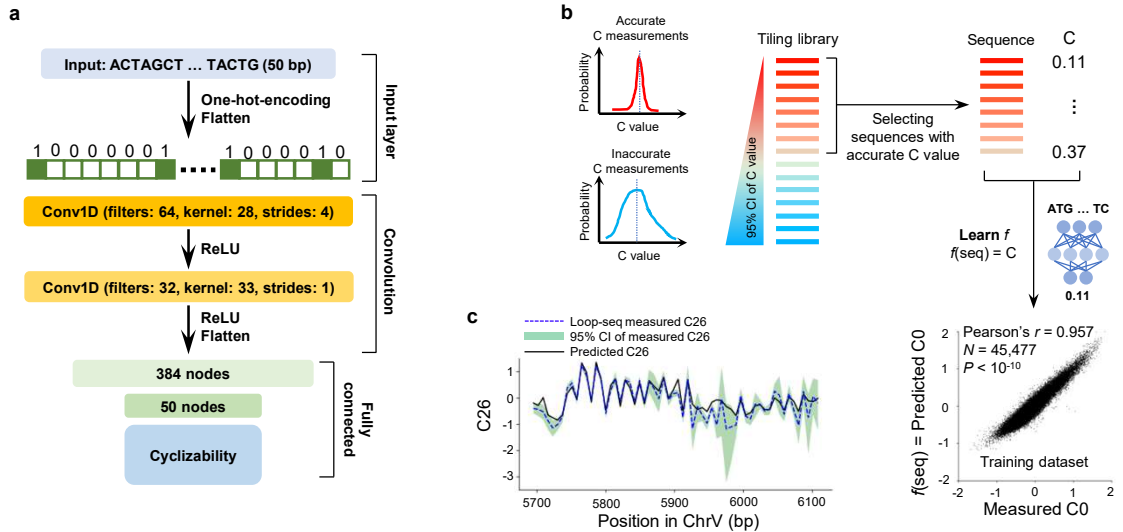
Fig. 4



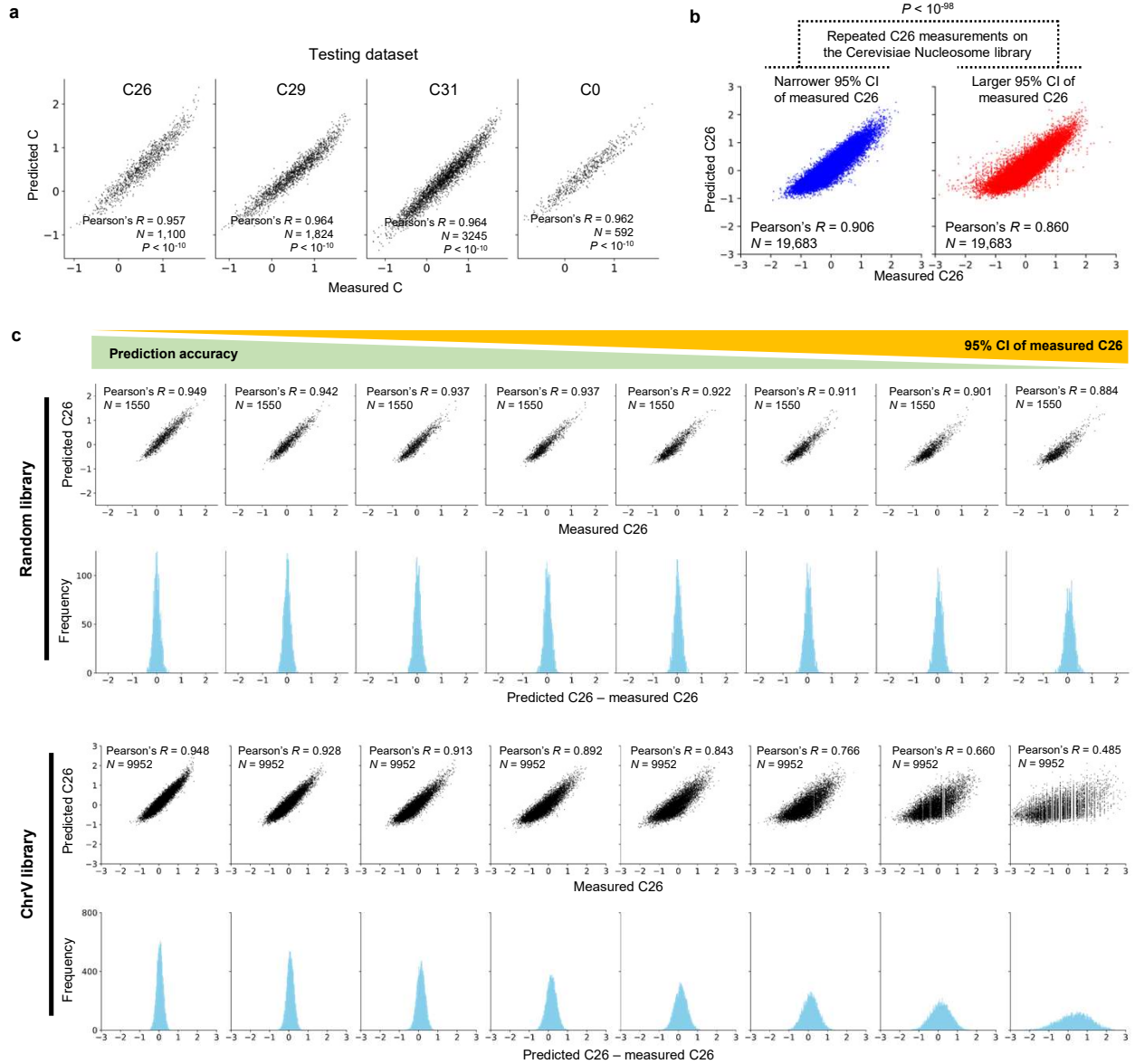
Supplementary Fig. 1



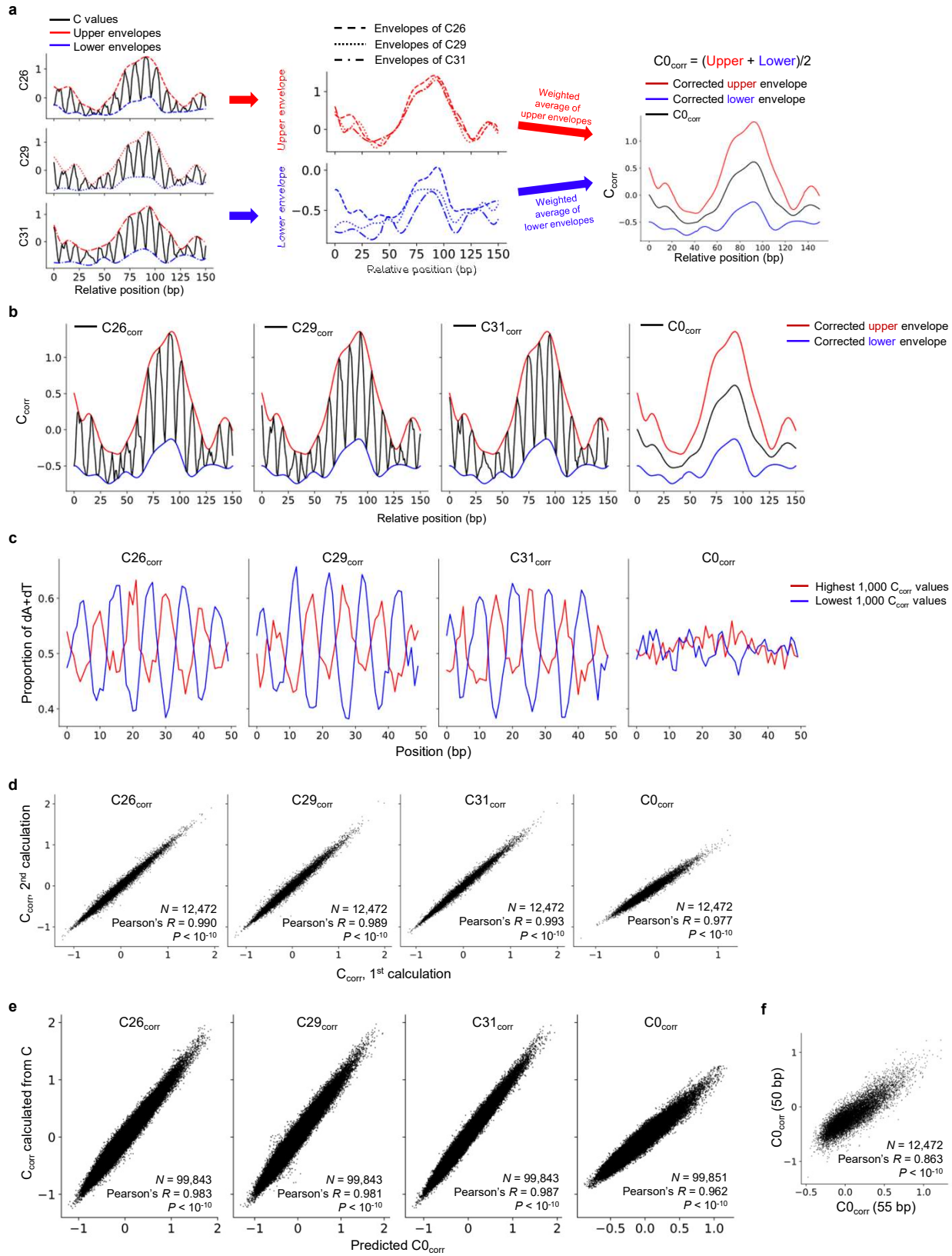
Supplementary Fig. 2



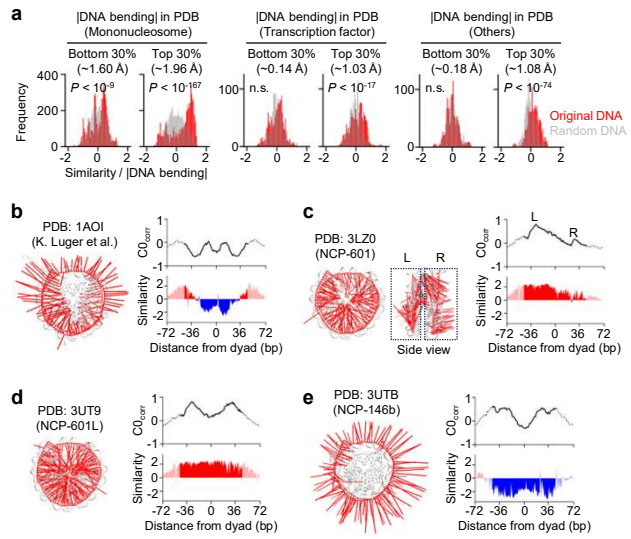
Supplementary Fig. 3



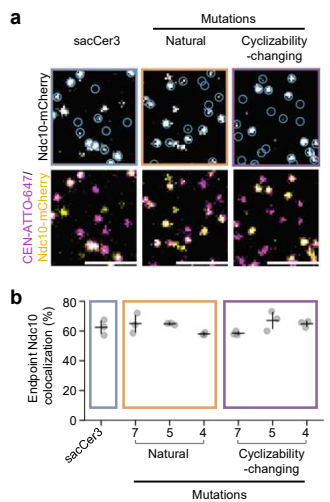
Supplementary Fig. 4



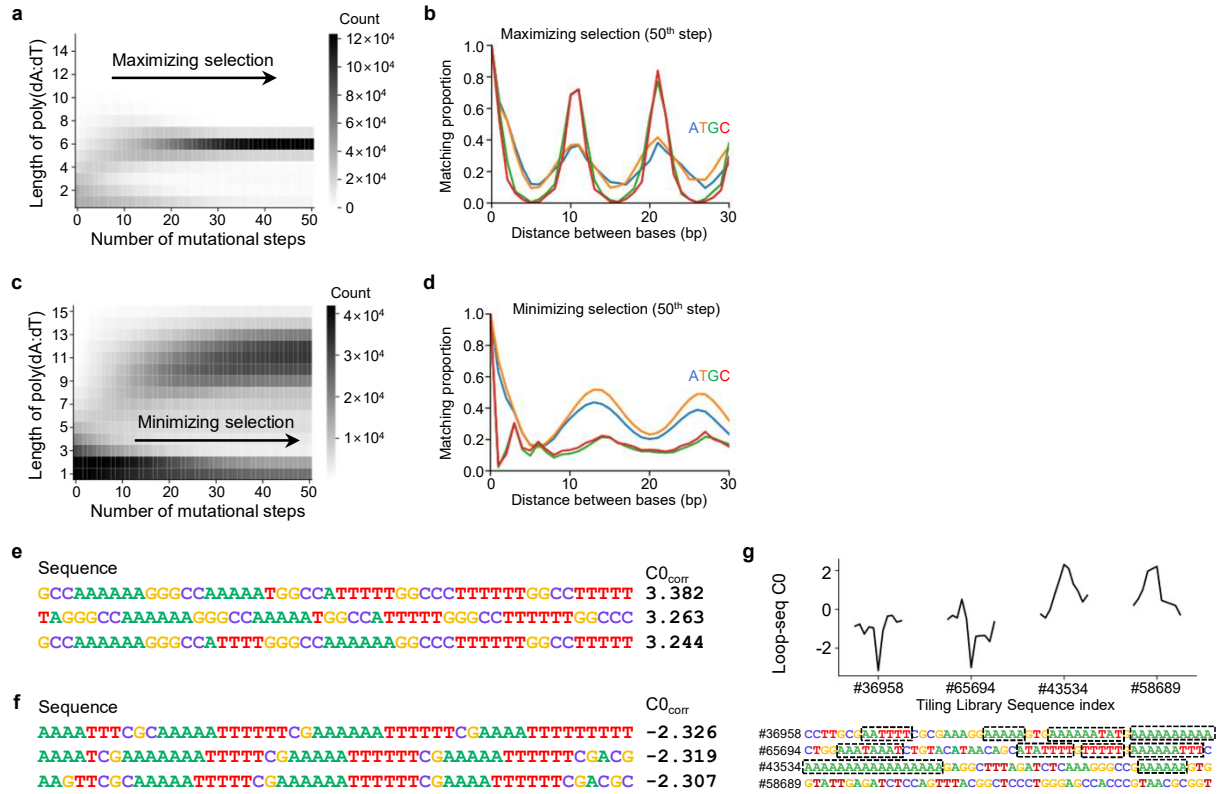
Supplementary Fig. 5



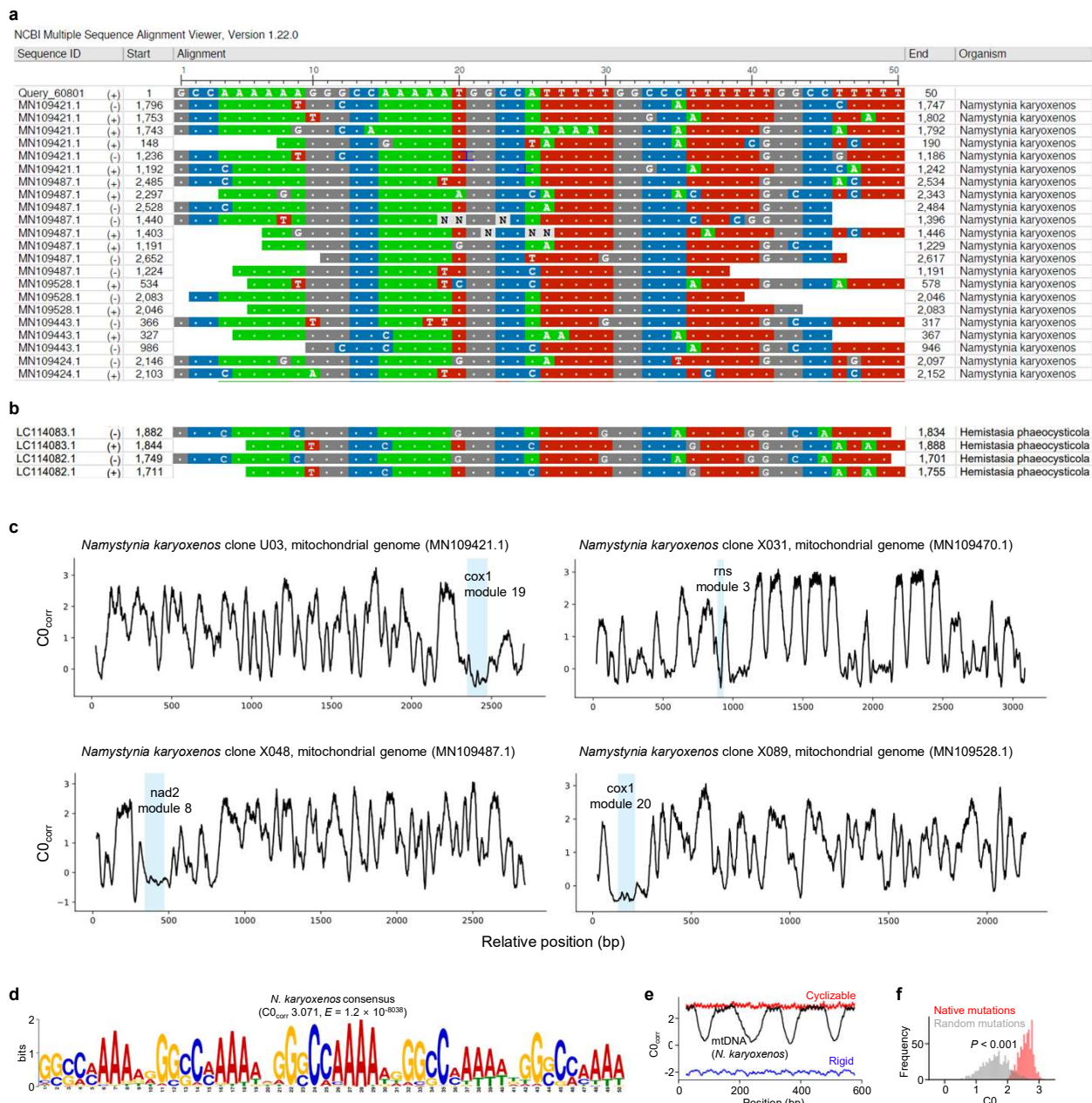
Supplementary Fig. 6



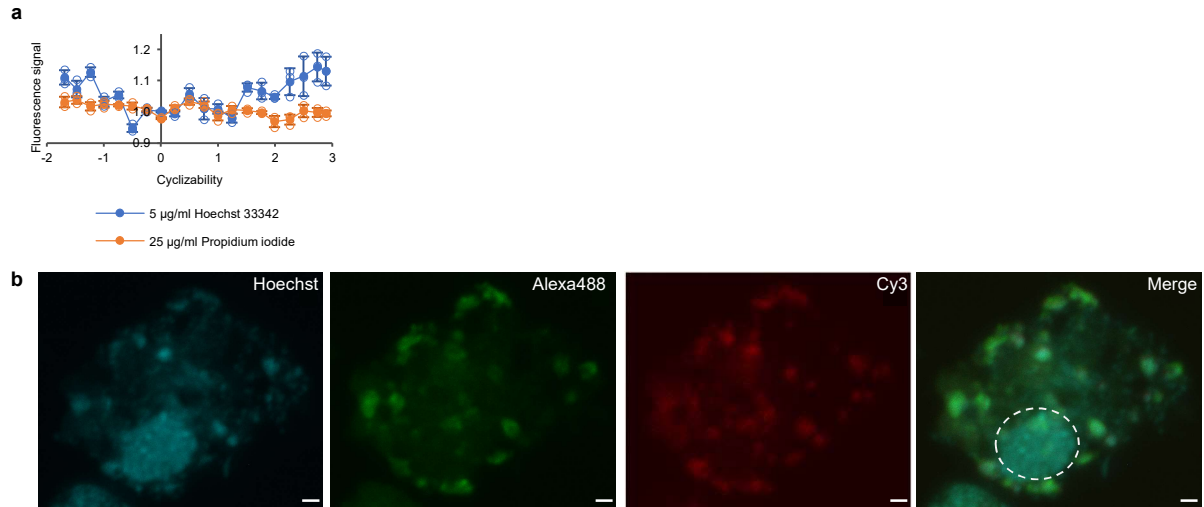
Supplementary Fig. 7



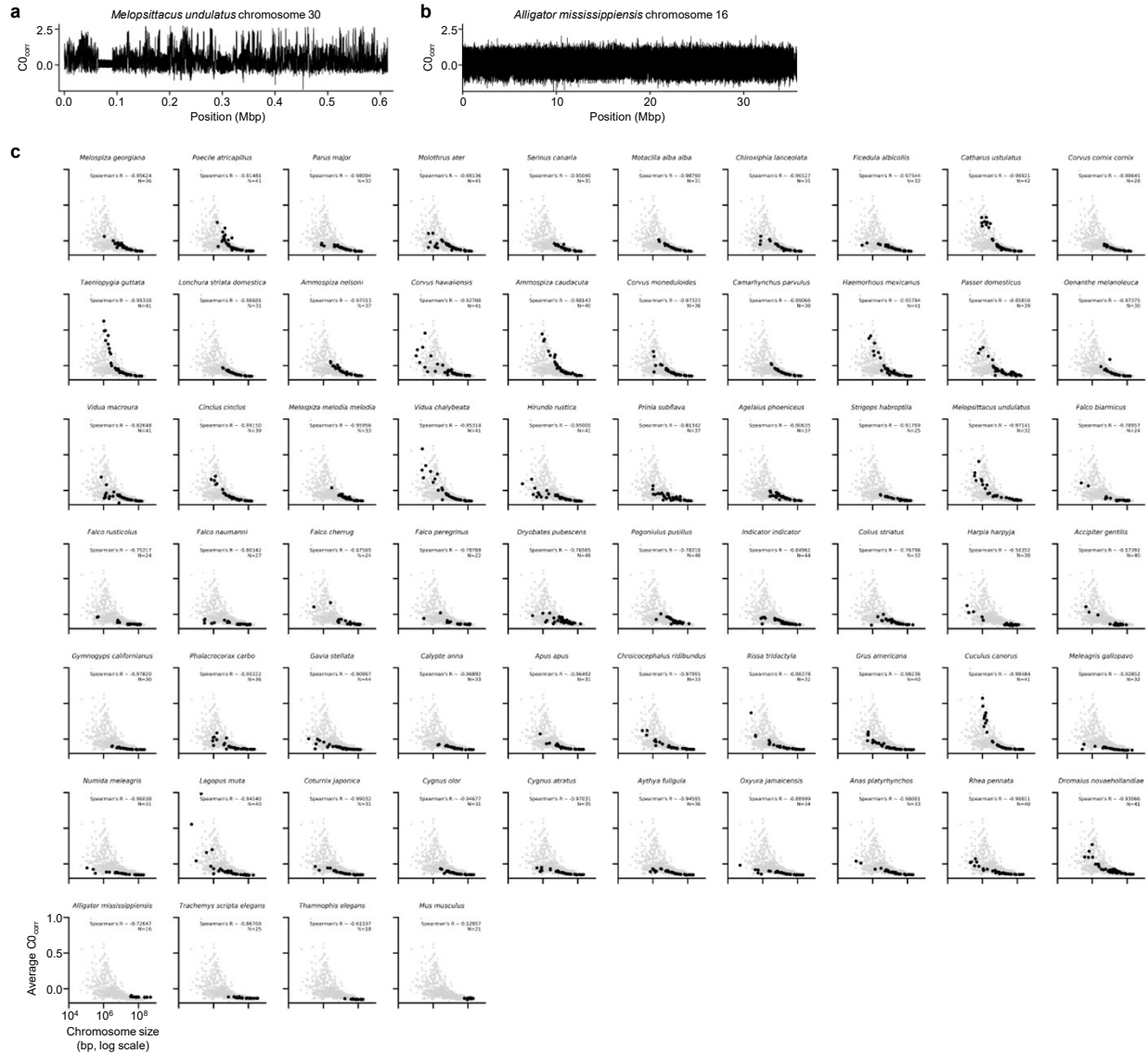
Supplementary Fig. 8



Supplementary Fig. 9



Supplementary Fig. 10



Supplementary Fig. 11